ACS OMEGA

Open Access

http://pubs.acs.org/journal/acsodf

Article

Diverse Self-Assembled Molecular Architectures Promoted by C−H···O and C−H···Cl Hydrogen Bonds in a Triad of α-Diketone, α-Ketoimine, and an Imidorhenium Complex: A Unified Analysis Based on XRD, NEDA, SAPT, QTAIM, and IBSI Studies

Ankita Sinha, Suphal Sen, Tejender Singh, Aniruddha Ghosh, Satyen Saha, Krishanu Bandyopadhyay, Arindam Dey, Suparna Banerjee,* and Jaydip Gangopadhyay*

Cite This: *ACS Omega* 2024, 9, 45518−45536

Read Online

ACCESS | Metrics & More | Article Recommendations | Supporting Information

ABSTRACT: X-ray structural elucidation, supramolecular self-assembly, and energetics of existential noncovalent interactions for a triad comprising α-diketone, α-ketoimine, and an imidorhenium complex are highlighted in this report. Molecular packing reveals a self-assembled 2D network stabilized by the C−H···O H-bonds for the α-diketone (benzil), and the first structural report of Brown and Sadanaga stressing on the prevalence of *only the van der Waals forces* seems to be an oversimplified conjecture. In the α-ketoimine, the imine nitrogen atom undergoes intramolecular N···H interaction to render itself inert toward intermolecular C−H···N interaction and exhibits two types of C−H···O H-bonds in consequence to generate a self-assembled 2D molecular architecture. The imidorhenium complex features a self-aggregated 3D packing engendered by the interplay of C−H···Cl H-bonds along with the ancillary C−H···π, C···C, and C···Cl contacts. To the best of our knowledge, in rhenium chemistry, this imidorhenium complex unravels the first example of self-associated 3D molecular packing constructed by the directional hydrogen bonds of C−H···Cl type. The presence of characteristic supramolecular synthons, viz., $R_2^2(12)$, $R_2^2(16)$, and $R_2^2(14)$, in the α-diketone, α-ketoimine, and imidorhenium complex, respectively, has prompted us to delve into the energetics of noncovalent interactions. Symmetry-adapted perturbation theory analysis has authenticated a stability order: $R_2^2(14) > R_2^2(12) > R_2^2(16)$ based on the interaction energy values of −25.97, −9.93, and −4.98 kcal/mol, respectively. The respective average contributions of the long-range dispersion, electrostatic, and induction forces are 58.5, 32.8, and 8.7%, respectively, for the intermolecular C−H···O interactions. The C−H···Cl interactions experience comparable contribution from the dispersion force (57.9% on average), although the electrostatic and induction forces contribute much less, 28.0 and 14.1%, respectively, on average. The natural energy decomposition analysis has further attested that the short-range, interfragment charge transfer occurring via the lp(O/Cl) → σ*(C−H) routes contributes 17−25% of the total attractive force for the C−H···O and C−H···Cl interactions. Quantum theory of atoms in molecules analysis unfolds a first-order exponential decay relation ($y = 8.1043e^{-x/0.4095}$) between the electron density at the bond critical point and the distance of noncovalent interactions. The distances of noncovalent interactions in the lattices are internally governed by the individual packing patterns rather than the chemical nature of the H-bond donors and acceptors. Intrinsic bond strength index analysis shows promise to correlate the electron density at BCP with the SAPT-derived interaction energy for the noncovalent interactions. Two factors: (i) nearly half the HOMO−LUMO energy difference for the imidorhenium complex (∼30 kcal/mol) compared to the organics, and (ii) ∼60% localization of HOMO over the *mer*-$ReCl_3$ moiety clearly indicate an enhanced polarizability of the complex facilitating the growth of weak C−H···Cl H-bonds.

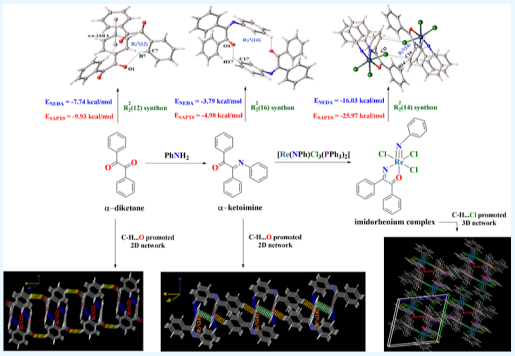

1. INTRODUCTION

While the molecular structure is dictated by the covalent bonds, the molecular packing pattern in the solid state is governed by an intricate interplay of directional noncovalent interactions. The quintessential contributor among the noncovalent interactions is the hydrogen bond (H-bond) having strength usually in the range of 2−25 kcal/mol.[1] Alongside various hydrogen bonds, other noncovalent forces like C−H···π,[2,3] ion−π,[4−7] lone pair−π,[8,9] π−π,[10−12] σ−hole,[13−15] and π−hole[16−19] interactions have been authenticated to play indelible roles in multifarious activities such as protein

Received: August 20, 2024
Revised: October 21, 2024
Accepted: October 23, 2024
Published: November 2, 2024

Scheme 1. Layout for the Synthesis of α-Ketoimine and Imidorhenium(V) Complex from the α-Diketone

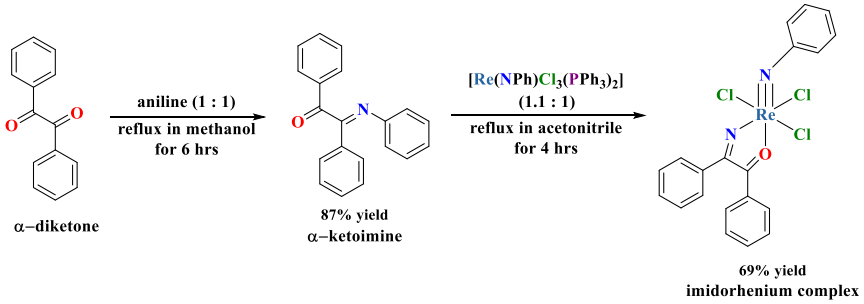

design,[20] enzyme activity,[21,22] ion/electron/proton transportation,[23−26] molecular recognition,[27−29] inclusion complexes,[30,31] luminescent efficacy,[32,33] and supramolecular construction.[34,35]

Although the archetypal, moderate-to-strong, classical H-bonds D−H···A (D = A = O/N/F) are well-acclaimed since their inception, the widespread C−H···O interactions were ignored in the context of hydrogen bonding until Sutor's seminal crystallographic study published in 1962−63.[36,37] Through a strenuous journey for recognition embracing all the dissents and criticisms,[38] the nonclassical C−H···O interactions have been proclaimed as the attractive H-bonds in 1982 after the extensive crystallographic survey done by Taylor and Kennard.[39] Unfortunately, even today, the C−H···O interactions are often overlooked or underestimated in common parlance when coexisting with other strong H-bonds. Despite that, the chemistry of C−H···O bonds never remains researchers' out-of-focus due to its profound significance in the biological domain.[40−42] In supramolecular chemistry also, a proclivity for analyzing the innate features of crystal packing, self-assembly, and structure-energy correlation sustains for those molecules enriched with C−H···O bonds.

By the time, the C−H···O interaction had earned the status of genuine H-bond,[43,44] another frequently encountered supramolecular force, viz., the C−H···Cl interaction, was still struggling to be unanimously categorized as the H-bond even in 1995.[45] With the growing consensus in opinions, especially in the last three years of the twentieth century (1997−1999),[46−50] the C−H···Cl interactions had earned the repute of true H-bonds. We have noted that, barring the organic and organometallic compounds, much less attention has been devoted to the C−H···Cl interactions in inorganic compounds with a focus to analyze their structure−energy interrelationship. Therefore, prudent exploitation of the electronically versatile metal-Cl bonds as C−H bond acceptors has a rich prospect in crystal engineering.

Since prospect invokes interest, we have shown interest in self-assembled networks crafted by the metal−halogen bonds as the H-bond acceptors, and this work has been realized with a triad of compounds: α-diketone (benzil), its monoimine derivative (α-ketoimine), and an α-ketoimine-bound imidorhenium(V) complex. A synthetic layout is provided in Scheme 1 for a glimpse. Imidorhenium complexes have been recognized as the enterprising species in rhenium chemistry, and the chelation of a plethora of ligands such as azoimine,[51] imineoxime,[51] pyridyloxime,[51] azopyridine,[52] azopyrimidine,[53] pyridyltriazines,[54] pyrazinyltriazine,[54] pyridylimine,[55] pyridylazole,[56] salicylideneimine,[57] β-ketoimine,[58] diazabutadiene,[59] hydrotris(pyrazolyl)borate,[60] *N*,*N*-diethylbenzoylthiourea,[61] *N*,*N*-diethyl-*N*′-benzoyliminothiourea,[61] cyclam,[62] corrole,[63] etc., to imidorhenium moiety are known. However, apart from this report, binding of α-ketoimine to the imidorhenium(V) motif has not been previously published.

Molecular packing reveals exclusive occurrence of the C−H···O type of H-bonds both in the α-diketone and α-ketoimine to engender self-assembled two-dimensional (2D) molecular architecture in each of them. Aiming to design supramolecular networks in rhenium complexes through the involvement of C−H···Cl−M type of H-bonds, we have judiciously opted for $[Re^{V}(NPh)Cl_3(PPh_3)_2]$ precursor over the well-explored $[Re^{I}(CO)_5Cl]$. The precursor, we have chosen seems promising since the Cl atoms can act as the only H-bond acceptors in absence of free terminal oxygen atoms. Indeed, the imidorhenium(V) complex reported herein exclusively manifests C−H···Cl interactions as the H-bonds to engender self-aggregated, three-dimensional (3D) molecular packing. To the best of our knowledge, apart from this imidorhenium complex, there is no precedence of self-association promoted only by the C−H···Cl hydrogen bonds in rhenium chemistry.

Recognition of several fascinating $R_2^2(12)$, $R_2^2(16)$, and $R_2^2(14)$ supramolecular synthons in the triad has insisted us to thoroughly examine the physical aspects of interaction energy of traditionally weak C−H···O and C−H···Cl interactions. Moreover, we have scrutinized other supramolecular forces like C−H···π, π−π, and C···C interactions to afford a comprehensive understanding of noncovalent energetics in the lattices. For this purpose, we have resorted to energy decomposition analysis (EDA), namely, the natural energy decomposition analysis (NEDA)[64−66] and symmetry-adapted perturbation theory (SAPT)[67] analysis. Topological properties of electron density pertinent to the noncovalent interactions in real space have also been analyzed through quantum theory of atoms in molecules (QTAIM).[68,69] Inherent electronic features of the noncovalent interactions have been additionally probed via the intrinsic bond strength index (IBSI) analysis.[70] With such revelations, we expect that nontraditional H-bonds can be rationally put to use to design self-assembled versatile architectures in the realm of variable-valent rhenium chemistry.

2. EXPERIMENTAL SECTION

2.1. Materials and Physical Measurements. The reagents, such as, triphenylphosphine, benzil, and aniline, have been procured from Avra Synthesis, and $KReO_4$ has been purchased from Thermo Fisher Scientific. Following the standard procedures, commercially available solvents were dried and distilled before usage. The starting materials, i.e., $[ReOCl_3(PPh_3)_2]$ and $[Re(NC_6H_5)Cl_3(PPh_3)_2]$, have been synthesized following the reported procedures.[71,72] Since all the compounds are stable in air, an inert atmosphere has not been maintained in any synthesis.

https://doi.org/10.1021/acsomega.4c07702
ACS Omega 2024, 9, 45518−45536

Table 1. Selected Crystallographic Data and Refinement Parameters of the Triad

compound	α-diketone	α-ketoimine	imidorhenium complex
formula	$C_{14}H_{10}O_2$	$C_{20}H_{15}NO$	$C_{26}H_{20}Cl_3N_2ORe$
M (g/mol)	210.234	285.33	668.99
temperature/K	298	273.15	100.15
crystal system	trigonal	triclinic	triclinic
space group	$P3_221$	$P\bar{1}$	$P\bar{1}$
crystal size (mm)	0.15 × 0.13 × 0.03	0.28 × 0.15 × 0.03	0.2 × 0.1 × 0.1
a (Å)	8.3999(8)	8.3837(7)	9.3733(5)
b (Å)	8.3999(8)	9.4195(10)	12.1457(8)
c (Å)	13.6693(16)	10.4823(10)	12.4168(5)
α, β, γ (deg)	90, 90, 120	74.184(3), 76.721(3), 82.985(3)	68.729(5), 71.300(4), 76.113(5)
V (Å^3), Z	835.27(15), 3	773.59(13), 2	1235.44(13), 2
ρ_{calc} g/cm^3	1.254	1.225	1.798
μ/mm^{-1}	0.083	0.075	5.264
Θ range for data collection/deg	3.17−30.64	2.063−29.678	2.136−27.062
index ranges	$-12 \le h \le 12$, $-12 \le k \le 12$, $-19 \le l \le 19$	$-11 \le h \le 11$, $-13 \le k \le 13$, $-14 \le l \le 14$	$-11 \le h \le 11$, $-15 \le k \le 15$, $-15 \le l \le 15$
total, uniq. data, R_{int}	64681, 1705, 0.2571	34918, 4364, 0.0696	17430, 5077, 0.0622
$R1$, $\omega R2$, S	0.0333, 0.1001, 1.0201	0.0443, 0.1194, 1.006	0.0368, 0.0643, 1.040
largest diff. peak/hole/eÅ^{-3}	0.1535/−0.1776	0.156/−0.118	1.249/−1.479
radiation (Å)	Mo−Kα, 0.71073	Mo−Kα, 0.71073	Mo−Kα, 0.71073

The NMR spectra have been recorded on a Bruker Avance III-500 MHz spectrometer in $CDCl_3$ solvent. The spin−spin structures have been abbreviated as d, doublet; t, triplet; and m, aromatic multiplet. The IR spectra have been analyzed with a PerkinElmer FTIR spectrometer (10.7.2 version). A Perkin−Elmer 2400 II elemental analyzer has been used for the microanalysis purpose. Melting points have been recorded manually using the sulfuric acid bulb.

2.2. Synthesis of the α-Ketoimine. 2.1 g (10 mmol) of the α-diketone (benzil) was dissolved in 25 mL of methanol containing one drop of acetic acid, followed by dropwise addition of 0.93 g (10 mmol) of aniline into the solution over a period of 10 min with gradual shaking. The resulting light yellow mixture was then refluxed for 6 h. The solution turned bright yellow in color, and its volume was then reduced to 15 mL. Upon overnight cooling at ambient temperature, the solution afforded a bright yellow crystalline product. Single crystals were obtained through slow evaporation at room temperature from a methanolic solution of the crystalline compound.

2.2.1. Analytical Data of the α-Ketoimine. Yield: 2.48 g (87%). Anal. Calcd for $C_{20}H_{15}NO$: C, 84.11; H, 3.50; N, 4.90. Found: C, 83.96; H, 3.42; N, 4.78. FT-IR (cm^{-1}): 3062 (m, $\nu_{C-H(stretch)}$), 1659 (vs, $\nu_{C=O}$), 1591 (s, $\nu_{C=N}$), 1449 (m, $\nu_{C=C}$); ^{1}H NMR (δ, ppm): 8.00 (d, J = 10 Hz, 2H), 7.91 (d, J = 10 Hz, 2H), 7.78 (d, J = 10 Hz, 2H), 7.69 (t, J = 10 Hz, 1H), 7.54 (t, J = 7.5 Hz, 1H), 7.47 (t, J = 7.5 Hz, 1H), 7.36 (t, J = 10 Hz, 1H), 7.15 (t, J = 10 Hz, 2H), 6.90−6.97 (m, 3H). mp 158−160 °C.

2.3. Synthesis of the Imidorhenium Complex. 46 mg (0.05 mmol) of $[Re(NC_6H_5)Cl_3(PPh_3)_2]$ was partially dissolved in 35 mL of acetonitrile to make a bottle green suspension, into which 16 mg (0.055 mmol) of α-ketoimine dissolved in 5 mL of acetonitrile was then added. The mixture was heated to reflux for 4 h. By this time, the solution gradually turned dark brown in color. The solvent was then removed under reduced pressure and washed three times (10 mL each) with hexane. The dark mass thus obtained was then subjected to column chromatography on a silica gel bed (25 × 1 cm, 60−120 mesh). A brown band was eluted with a benzene−acetonitrile (12:1) mixture. Solvent removal from the eluate under reduced pressure afforded a brown-colored $[Re(NC_6H_5)Cl_3(\alpha\text{-ketoimine})]$ complex. Single crystals were obtained from slow diffusion of dichloromethane solution of the complex into hexane inside a refrigerator.

2.3.1. Analytical Data of the Imidorhenium Complex. Yield: 23 mg (69%). Anal. Calcd for $C_{26}H_{20}Cl_3N_2ORe$: C, 46.63; H, 2.99; N, 4.18. Found: C, 46.86; H, 2.73; N, 4.08. FT-IR (cm^{-1}): 2924 (m, $\nu_{C-H(stretch)}$), 1725 (m, $\nu_{C=O}$), 1671 (m, $\nu_{C=N}$), 1421 (m, $\nu_{C=C}$), 897 (vs, $\nu_{Re=N}$),; ^{1}H NMR (δ, ppm): 8.01 (d, J = 5.0 Hz, 2H), 7.69 (t, J = 10 Hz, 2H), 7.54 (t, J = 7.5 Hz, 2H), 7.48 (t, J = 7.5 Hz, 1H), 7.07 (d, J = 7.5 Hz, 1H), 6.75 (d, J = 10 Hz, 1H), 6.21(d, 2H), 5.87(d, 4H), 5.32(d, 2H), 3.51(d, 3H). mp 184−186 °C.

2.4. X-ray Diffraction. Well-shaped single crystals of the triad have been selected for X-ray diffraction (XRD) on a Bruker D8 Quest diffractometer. From the structural data, the structures of α-ketoimine and imidorhenium complex have been generated by the SHELXT program[73] and refined subsequently by full matrix least-squares based on F^2 with the SHELXL package.[74,75] The structure of α-diketone has been generated by the SHELXS program[76] and refined by the Gauss−Newton method through the Olex2−1.5 package.[77] All of the hydrogen atoms of the three compounds have been located and treated by least-squares refinement. Anisotropic displacement parameters have been assigned to all the non-hydrogen atoms. Molecular graphics have been generated by using the Olex2−1.5 software suite.[77] Noncovalent interaction networks have been identified with the help of Mercury 4.0 software.[78] The crystallographic data reported in this paper have been deposited at the Cambridge Crystallographic Data Centre (CCDC), and the assigned reference numbers are 2322688, 2301468, and 2301469 for the α-diketone, α-ketoimine, and imidorhenium complex, respectively. Selected crystal data and refinement details of the triad have been summarized in Table 1.

2.5. Computational Methods. Gaussian 16, Revision C.01 program[79] has been used for the DFT calculations. The

https://doi.org/10.1021/acsomega.4c07702
ACS Omega 2024, 9, 45518−45536

Scheme 2. Feasibility of Different Synthetic Routes Attempted to Prepare the Imidorhenium(V) Complex from $[Re(NC_6H_5)Cl_3(PPh_3)_2]$ and $[ReOCl_3(PPh_3)_2]$ Precursors

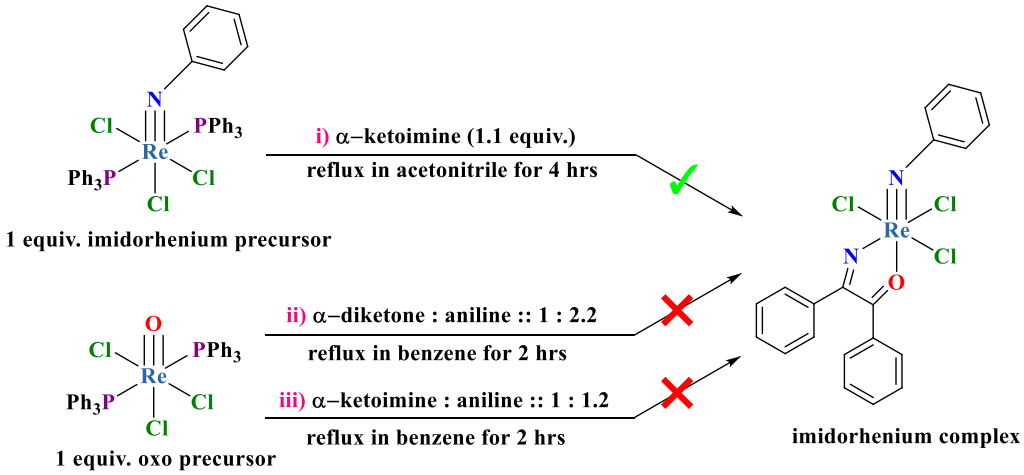

highly parameterized, empirical M06-2X exchange−correlation functional[80] with double the amount of nonlocal exchange (2X) has been entrusted by us for the DFT computations. It is the genuine performer within the 06 functionals for main group thermochemistry, kinetics, and noncovalent interactions.[80,81] The effect of dispersion force has been included in the computations with the Grimme dispersion correction functions (D3)[82] to effectively probe the electronic nature of the C−H···O, C−H···π, and C−H···Cl interactions. Since TZVP basis sets provide a required balance between the accuracy and computational performance satisfactorily, the def2-TZVP basis set[83] developed by the group of Ahlrichs has been employed in this study. Hence, the computational study has been accomplished at the trustworthy M06-2X-D3/def2-TZVP level of theory. We have used the crystallographic Cartesian coordinates derived from the olex2−1.5 program for the theoretical analysis of the noncovalent interactions in the triad. Cartesian coordinates pertinent to the α-diketone, α-ketoimine, and imidorhenium complex, and, of all the noncovalent interactions are provided in Tables S1−S15.

The Gauss-View 6.0 graphical interface[84] has been used to generate the input files as well as to interpret the results. Using the Multiwfn 3.8 software,[85] QTAIM analysis and IBSI analysis have been done at the M06-2X-D3/def2-TZVP level of theory. Decomposition of the interaction energy has been performed by the SAPT0 method using the correlation consistent jun-cc-pVDZ basis set[86] (except the metal) through the PSI4 electronic structure program package.[87] To implement RIFIT and JKFIT in SAPT0, the def2-tzvp-ri.gbs and def2-universal-jkfit.gbs basis sets have been, respectively, used for rhenium. NEDA has been performed using the NBO 7.0 program[88] patched with the Gaussian 16 suite. Energy analysis of the frontier molecular orbitals of the triad has been done using the *meta*-GGA M06L functional[89] at the M06L/def2-TZVP level of theory. Cartesian coordinates and total energy of the optimized triad at the M06L/def2-TZVP level of theory have been given in Tables S16−S18.

3. RESULTS AND DISCUSSION

3.1. Synthesis. Facile condensation between benzil and aniline in methanol has furnished a neutral α-ketoimine condensate (Scheme 1), which acts as a bidentate ligand toward the $[Re^V(NC_6H_5)Cl_3(PPh_3)_2]$ precursor, affording a brown-colored imidorhenium complex $[Re^V(NC_6H_5)Cl_3(\alpha$-ketoimine$)]$ under refluxing condition in acetonitrile for 4 h (path i of Scheme 2). We have also attempted two different *in situ* condensation methods (paths ii and iii of Scheme 2) in benzene using the $[ReOCl_3(PPh_3)_2]$ precursor. However, these two latter paths have resulted no tractable products of our concern. The futility of the *in situ* paths has been attributed to the well documented oxygen atom transfer ability of the $[ReO]^{3+}$ moiety toward the oxophilic PPh_3 group, which has eventually led to undesirable secondary reactions.

3.2. X-ray Structure Analysis. *3.2.1. α-Diketone.* Although the X-ray crystal structure of benzil had been first elucidated by Brown and Sadanaga almost 60 years ago,[90] followed by others' investigations,[91−96] none of these studies focus on the issue of C−H···O intermolecular H-bonds. Since the analysis of lattice packing and supramolecular pattern has undergone a vast transformation over the passage of time, we have felt the urge to re-examine its crystal structure. The *R*1 value in our case is converged at 3.33% compared to 7.8% in the previously reported[90] structure. With a much improved refinement factor, we have grabbed the opportunity to compare some selected bond parameters and other important structural attributes between the two independent structures.

The crystallographic 2-fold axis of each of the three benzil molecules present in a unit cell passes through the midpoint of the central carbon−carbon bond, and the asymmetric unit of the chiral-helical $P3_221$ space group effectively contains half of the benzil molecule. A symmetry-grown asymmetric unit containing the full benzil molecule is depicted in Figure 1, and selected bond parameters are collected in Table 2. In the solid

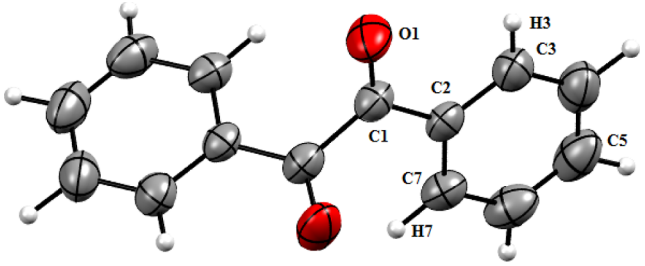

Figure 1. ORTEP view (30% probability ellipsoid) of the α-diketone (benzil) molecule along with the atom numbering scheme.

https://doi.org/10.1021/acsomega.4c07702
ACS Omega 2024, 9, 45518−45536

Table 2. Selected Bond Parameters of Two Structural Reports of α-Diketone for Comparison

geometrical attributes	α-diketone, our report	α-diketone, previous report[90]
$C_{keto}(sp^2)-C_{keto}(sp^2)$ length (Å)	1.526(2)	1.533
$C_{keto}(sp^2)-C_{phenyl}(sp^2)$ length (Å)	1.466(2)	1.486
C=O length (Å)	1.214(2)	1.219
mean C−C length in the phenyl ring (Å)	1.372	1.398
dihedral angle between two phenyl groups (deg)	75.54	70
O=C−C=O torsion angle (deg)	−108.0(2)	—

state, the α-diketone appears to be twisted around the central $C_{keto}(sp^2)-C_{keto}(sp^2)$ single bond. As evident from the torsion angle of −108(2)° along the $O=C_{keto}-C_{keto}=O$ atomic array, two O centers are oriented in an anticlinal fashion, and that indicates a nonplanar $O=C_{keto}-C_{iketo}=O$ fragment (r.m.s. deviation of ∼0.278 Å from planarity). However, individual O=C(Ph) fragments are appreciably planar (rmsd, 0.026 Å), and the torsion angle for the atomic sequence, $O(1)-C(1)-C_{ipso}(2)-C_{ortho}(3)$, is only 3.7(2)°. An acute dihedral angle of 75.54° between the two phenyl groups of the O=C(Ph) fragments corroborates an angular disposition of the benzoyl fragments. All the bond lengths fall within the normal range in our case, but a uniform reduction has been observed compared to the initial report of Brown and Sadanaga.[90]

3.2.2. α-Ketoimine. The structure of the α-ketoimine had been reported earlier[97] for the purpose of analyzing the flexibility of its molecular conformations. We are also interested in this compound from two completely different perspectives: firstly to delve into the existing noncovalent interactions and secondly to explore its coordination ability with imidorhenium(V) species. For these reasons, we have prepared the α-ketoimine by simple Schiff-base condensation, avoiding an arduous procedure based on oxidative coupling of amine adopted by Guner et al.[97] The α-ketoimine has been crystallized in the symmorphic space group $P\bar{1}$ of the triclinic system. Since reflection, proper rotation axis, and rotoinversion axis of order 2 and beyond are absent in the triclinic system, the screw axis and glide plane are also nonexistent. Therefore, the reduction in crystal symmetry compared to the α-diketone should influence the structural attributes and molecular packing of the α-ketoimine. These aspects have been highlighted in the following discussion.

Twisted α-ketoimine exists exclusively in the *Z*-isomeric form (solid state), as shown in the asymmetric unit given in Figure 2. Selected bond parameters of our structure and the previous one[97] have been collected in Table 3. Conspicuous structural changes accompanied by the α-diketone → α-ketoimine transformation are: (i) an anticlinal orientation of the O and N donor centers along the $O=C_{keto}-C_{imine}=N$ sequence in the α-ketoimine has been authenticated from a torsion angle of −95.4(2)°, which is reduced by ca. 13° compared to the torsion angle of the $O=C_{keto}-C_{keto}=O$ skeleton in the α-diketone; (ii) similar to the $O=C_{keto}-C_{keto}=O$ framework of the α-diketone, the $O=C_{keto}-C_{imine}=N$ fragment is also nonplanar (r.m.s. deviation of 0.242 Å from planarity) but to a lesser extent than the former by 0.036 Å; (iii) as reflected from the dihedral angle values (Table 3) between the phenyl rings of the α-ketoimine, it adopts a three-blade propeller structure when viewed along the central $C_{keto}(sp^2)-C_{imine}(sp^2)$ bond unlike the angular α-diketone;

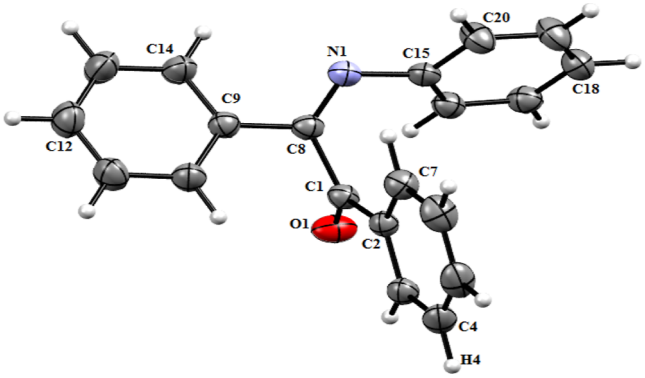

Figure 2. ORTEP view (30% probability ellipsoid) of the asymmetric unit of the α-ketoimine molecule with the atom numbering scheme.

Table 3. Selected Bond Parameters of the α-Ketoimine (in Our and Previous[97] Reports) and Their Corresponding Values in the Imidorhenium(V) Complex for Comparison

bond parameters	α-ketoimine, our report	α-ketoimine, previous report[97]	imidorhenium complex
C1−O1 (Å)	1.215(2)	1.214(2)	1.281(6)
C8−N1 (Å)	1.275(2)	1.278(2)	1.340(7)
C1−C8 (Å)	1.521(2)	1.522(2)	1.445(6)
C1−C2 (Å)	1.475(2)	1.477(2)	1.471(8)
C8−C9 (Å)	1.482(2)	1.478(2)	1.470(6)
N1−C15 (Å)	1.426(2)	1.422(2)	1.446(6)
torsion angle of the $O=C_{keto}-C_{imine}=N$ array (deg)	−95.4(2)	95.5(2)	5.4(6)
dihedral angle between C2−C7 and C9−C14 motifs (deg)	87.96	—	75.46
dihedral angle between C9−C14 and C15−C20 motifs (deg)	80.85	—	63.51
dihedral angle between C15−C20 and C2−C7 motifs (deg)	79.03	—	88.49

and (iv) the $O(1)-C(1)-C_{ipso}(2)-C_{ortho}(3)$ torsion angle is −8.4(2)° in the α-ketoimine, and the O=C(Ph) fragment is nearly planar (rmsd, 0.027 Å) similar to the α-diketone. In contrast, impacted by the imine functionalization, the torsion angle for the $N(1)-C(8)-C_{ipso}(9)-C_{ortho}(10)$ array becomes −160.9(2)° and suggests an accountable deviation from planarity (rmsd, 0.092 Å) for the N=C(Ph) motif.

3.2.3. Imidorhenium Complex. The asymmetric unit of the imidorhenium(V) complex is depicted in Figure 3a, and the selected bond parameters are collected in Table 4. In the octahedral complex $[Re^{V}(NC_6H_5)Cl_3(\alpha\text{-ketoimine})]$, the *mer*-$ReCl_3$ moiety and the imine nitrogen atom (N1) constitute the equatorial plane, from which the rhenium atom is shifted upward to the phenylimido nitrogen atom (N2) by 0.23 Å. Since the N2 atom is a potential π-donor, the $Re^{V}(NC_6H_5)$ fragment is multiply bonded, and consequently, the axial Re1−N2 bond is ∼0.31 Å shorter than the equatorial Re1−N1 linkage. Expectedly, the Re1−Cl1 bond lying *trans* to the weak π-acceptor N1 atom is the shortest among the three metal-chloride bonds. The bite angle of α-ketoimine in the complex is only 74.0(1)°. The axial angle, in consequence, has been significantly reduced to 166.4(1)° to adjust such a five-member strained chelate ring. Both the C=O and C=N lengths are

https://doi.org/10.1021/acsomega.4c07702
ACS Omega 2024, 9, 45518−45536

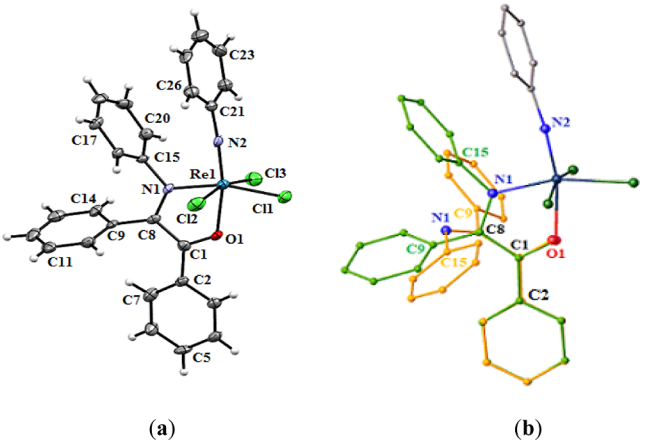

(a) (b)

Figure 3. (a) ORTEP view (30% probability ellipsoid) of the asymmetric unit of the imidorhenium complex with atom numbering scheme, and (b) overlay diagram of free α-ketoimine (yellow) and chelated α-ketoimine (green) in the imidorhenium complex.

Table 4. Selected Bond Parameters of the Imidorhenium(V) Complex

bond length (Å)		bond angle (deg)	
Re1−Cl1	2.342(1)	Cl1−Re1−Cl3	87.87(3)
Re1−Cl2	2.359(1)	Cl1−Re1−Cl2	86.53(5)
Re1−Cl3	2.350(1)	Cl2−Re1−Cl3	166.25(5)
Re1−N1	2.012(3)	O1−Re1−N2	166.4(1)
Re1−N2	1.706(4)	N1−Re1−O1	74.0(1)
Re1−O1	2.068(4)	N1−Re1−Cl1	163.9(1)

increased by ∼0.07 Å, and the length of the C1−C8 bond is reduced by ∼0.08 Å in the complexed α-ketoimine compared to its free state. Although the electron-deficient Re^{V} center is not particularly suitable to favor π-acceptance by the ligand, the imido and chloro groups (π-donor) lying *trans* to the C═O and C═N functions, respectively, can facilitate the π-electron drift to some extent.

Affected by complexation, conformational changes of the phenyl rings in the ligand form a subject to scrutiny. For that purpose, an overlay diagram of the free and chelated α-ketoimine with superimposed O═C(Ph) groups is furnished in Figure 3b. It vividly displays two different positions of the imine nitrogen atom (N1) belonging to free and bound forms of α-ketoimine. The N1 atom lies on the opposite sides of the $C_{keto}(sp^2)-C_{imine}(sp^2)$ bond, as evident from the torsion angles of the $O{=}C_{keto}-C_{imine}{=}N$ fragment, −95.4(2)° and 5.4(6)° in the free and bound states, respectively. Therefore, chelation occurs through achieving a +synperiplanar position by the N1 atom with respect to the O1 atom of the free α-ketoimine via a clockwise rotation of ∼100° around the $C_{keto}(sp^2)-C_{imine}(sp^2)$ bond with subsequent spatial changes of the phenyl groups of the N═C(Ph) and C═N(Ph) motifs. Hence, Z → E geometrical isomerization is a requisite for the α-ketoimine ligand to form chelates.

3.3. Noncovalent Interactions in the Triad. With the primary aim to underscore the imperative role of noncovalent interactions in crafting the supramolecular architectures, we have analyzed the lattice packing pattern for the individuals of the triad. Characteristic supramolecular building blocks have been recognized and categorically represented in Figure 4 to facilitate the understanding of gross molecular packing as well as their energy properties (vide infra). All the existing intermolecular noncovalent interactions along with their geometric details are given in Table 5.

3.3.1. α-Diketone. The phenomenon of self-association through directional C−H···O hydrogen bonds, namely, C5−H5···O1 (Figure 4a) and C7−H7···O1 (Figure 4b), has been discernible in the solid state of benzil. A 12-member cyclic dimer with a $R_2^2(12)$ loop constructed by the intermolecular C7−H7···O1 hydrogen bonds is noted (Figure 4b). In the dimer, noncovalent $\pi-\pi$ stacking interaction is also present between the two tilted phenyl motifs, subtending a dihedral angle (angle between two plane−normals) of 7.92°. The ring normal and the vector between the ring centroids form an offset angle of 5.9°, and the centroid−centroid (Cg···Cg) distance is 3.848 Å. An eclipsing array of such cyclic dimers interlinked by C5−H5···O1 hydrogen bonds propagates across the crystallographic *b* axis to engender a one-dimensional (1D) framework mimicking a hollow channel. The hollow channels thus created are again vertically stacked via the intermolecular C5−H5···O1 bonds along the crystallographic *a* axis to finally form a two-dimensional (2D) columnar structure. The aforementioned supramolecular architecture is portrayed in Figure 5.

Since organic molecules with pure crystallographic screw axes are sparse, a view along the crystallographic *c* axis is worthwhile (Figure 6). It reveals groups of helical chains around the 3_2 screw axis. Our analysis has unraveled the unequivocal existence of directional C−H···O hydrogen bonds and $\pi-\pi$ stacking in the α-diketone lattice, while in Brown's report,[90] it had been claimed that *"The molecules pack together in the crystal with only van der Waals forces"*. Although it is logical to assume that both the C−H···O and $\pi-\pi$ supramolecular forces are principally stabilized by dispersion, there must be a significant contribution from the electrostatic and induction components (vide infra).

3.3.2. α-Ketoimine. As a notable structural feature, the imine N1 atom of the C═N(Ph) fragment in α-ketoimine is displaced downward from the phenyl ring (C15−C20) plane by 0.041 Å. A similar observation was reported earlier by Fukuyo and others in the case of aniline itself,[98] where the N atom lies out of the phenyl ring plane by ∼0.12 Å. We believe that this apparently benign downward movement of the N1 atom has far-reaching consequences: (i) the $C(15)_{ipso}-N1$ distance in free α-ketoimine is 0.034 Å longer than the analogous C−N bond of aniline, and that duly indicates a lesser conjugation of nitrogen lone pair with the phenyl π-system in α-ketoimine; (ii) allowing proximity between the N1 atom and the H14 atom to aid an establishment of N1···H14 intramolecular noncovalent contact ($d_{N1\cdots H14}$ = 2.57(2) Å, C14−H14···N1 angle = 97(1)°); and (iii) reduction in N1 lone pair availability due to formation of the N1···H14 contact thereby precludes further development of intermolecular C−H···N interaction. Consequently, the chance of a C−H···O bond-dominated molecular packing is augmented in the α-ketoimine akin to the α-diketone.

Indeed, α-ketoimine lattice packing exhibits intermolecular C−H···O bonds, as well as C−H···π, $\pi-\pi$, and C···C contacts, that in tandem build the self-associated supramolecular network. C17−H17···O1 bonds promote self-assembly between the two α-ketoimine molecules to generate a centrosymmetric dimer (Figure 4c). The graph set notation of the 16-member loop inside the dimer is $R_2^2(16)$. These loops are aligned in a parallel manner and mutually tethered by another type of C5−H5···O1 bonds (Figure 4d) to construct a

https://doi.org/10.1021/acsomega.4c07702
ACS Omega 2024, 9, 45518−45536

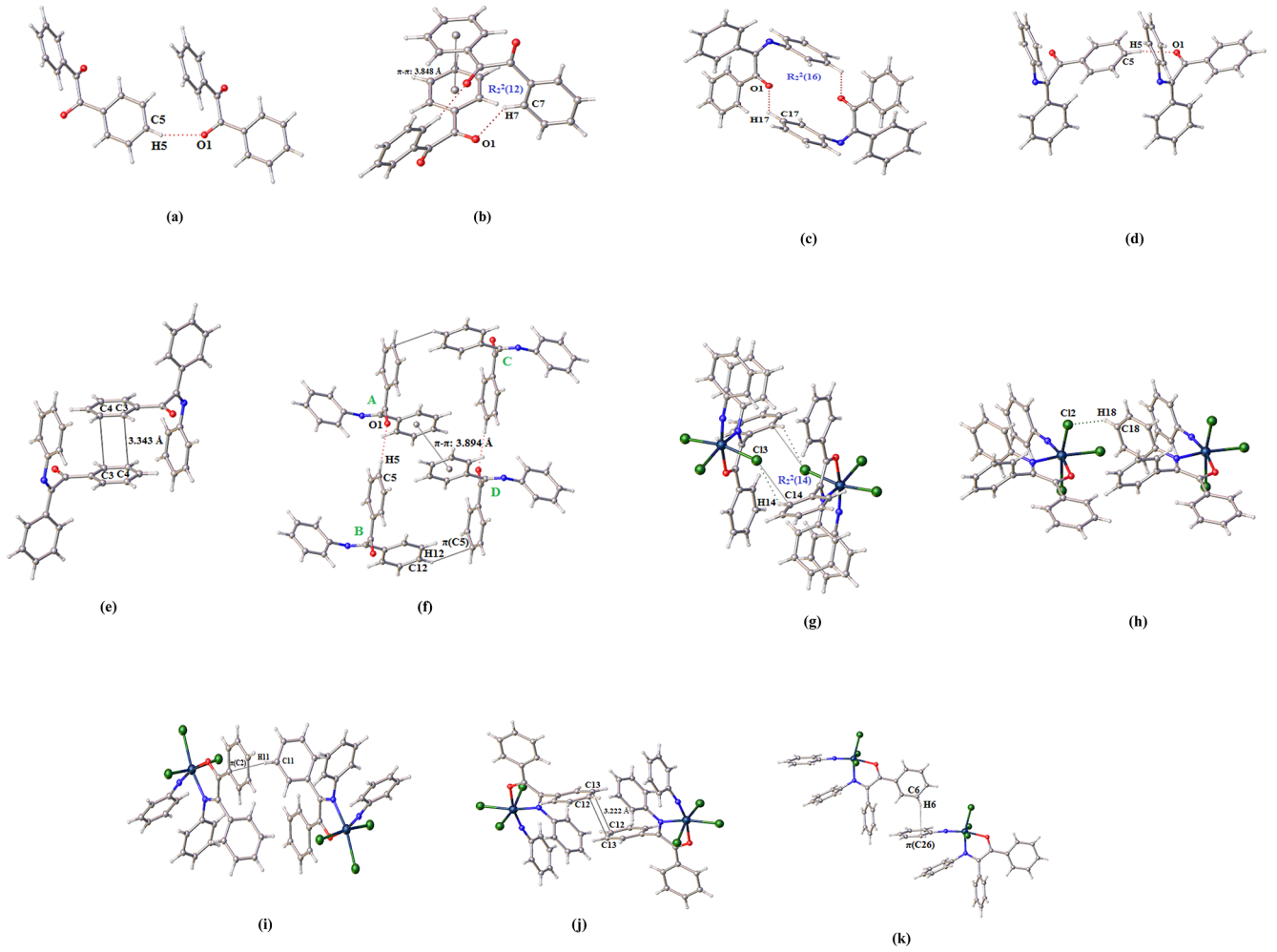

Figure 4. Versatile supramolecular structural blocks observed for the triad: (a,b) for the α-diketone, (c–f) for the α-ketoimine, and (g–k) for the imidorhenium complex. Symmetry codes: [(a) $-1 + x, +y, +z$], [(b) $-2 + y - x, -1 - x, 1/3 + z$], [(c) $-1 + x, +y, +z$], [(d) $-x, -y, 1 - z$], [(e) $1 - x, -y, 1 - z$], [(f) $1 - x, 1 - y, -z$], [(g) $1 - x, 1 - y, 1 - z$], [(h) $-1 + x, +y, +z$], [(i) $+x, -1 + y, +z$], [(j) $1 - x, 1 - y, -z$], [(k) $2 - x, 1 - y, -z$].

Table 5. Geometric Parameters of All the Intermolecular Noncovalent Interactions Prevailing in the Triad

chemical species	D–H···A	H···A (Å)	D···A (Å)	D–H···A (deg)
α-diketone	C7–H7···O1	2.49(1)	3.328(2)	141(1)
	C5–H5···O1	2.55(3)	3.444(3)	155(2)
	$\pi_{(C2-C7)}$–$\pi_{(C2-C7)}$	—	3.848 (Cg···Cg)	5.9 (offset)
α-ketoimine	C17–H17···O1	2.56(2)	3.234(4)	126(1)
	C5–H5···O1	2.46(2)	3.427(2)	169(2)
	C12–H12···π(C5)	2.80(2)	3.602(3)	139(1)
	$\pi_{(C9-C14)}$–$\pi_{(C9-C14)}$	—	3.894 (Cg···Cg)	20.2 (offset)
	C3···C4	—	3.343(2)	—
imidorhenium complex	C14–H14···Cl3	2.79(4)	3.293(4)	120(4)
	C18–H18···Cl2	2.87(5)	3.625(7)	147(3)
	C11–H11···π(C2)	2.84(5)	3.708(7)	171(4)
	C6–H6···π(C26)	2.86(3)	3.681(7)	158(3)
	C14···Cl3	—	3.293(4)	—
	C12···C13	—	3.222(7)	—

1D hollow channel along the crystallographic *a* axis. It is interesting to note that the parallelly disposed phenyl groups (C2–C7) of the O=C(Ph) fragments in the hollow channel are oriented in an edge(C3–C4)-to-edge(C4–C3) fashion (Figure 4e). This specific alignment is conducive for setting up a series of pairwise C3···C4 contacts (3.343(2) Å) to provide additional structural support to the channels.

Such hollow channels made up of $R_2^2(16)$ loops are vertically interlinked along the crystallographic *b* axis through an elegant interplay of C–H···π and π–π stacking interactions. The pendant phenyl groups (C9–C14) of the N=C(Ph)

https://doi.org/10.1021/acsomega.4c07702
ACS Omega 2024, 9, 45518–45536

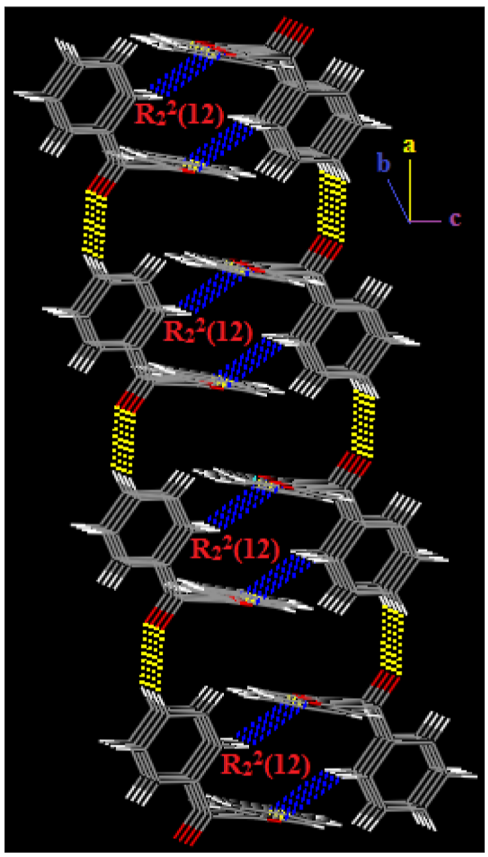

Figure 5. Intermolecular C5−H5···O1 hydrogen bond (yellow) assisted 2D vertical arrangement of 1D hollow channels made up of $R_2^2(12)$ loops (bounded by blue lines representing C7−H7···O1 hydrogen bonds) along the crystallographic *b* axis.

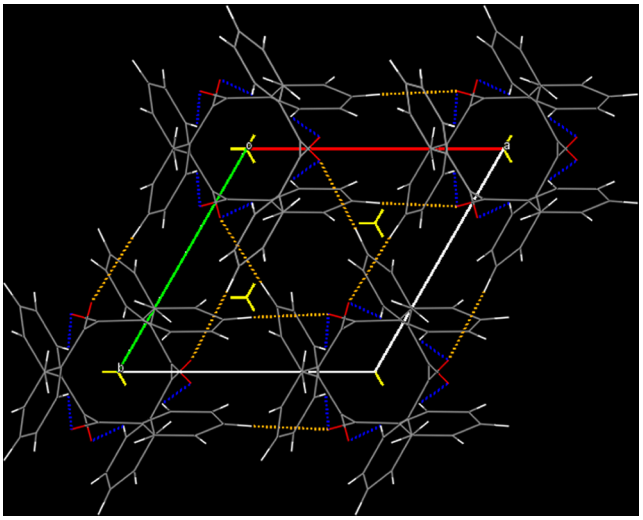

Figure 6. Groups of helical chains stabilized by the noncovalent C−H···O hydrogen bonds and $\pi-\pi$ interactions around the 3_2 screw axis (yellow arrow) when viewed along the crystallographic *c* direction.

motifs present in between two consecutive 1D hollow channels further participate in C12−H12···π(C5) interactions (AC or BD pair in Figure 4f), and also exhibit offset $\pi-\pi$ stacking (Cg···Cg = 3.894 Å, offset angle = 20.2°, A and D molecules in Figure 4f). Consequently, the directional interchannel cohesive interactions, viz., C12−H12···π(C5) and slipped $\pi-\pi$ stacking, finally afford a porous 2D columnar architecture (Figure 7).

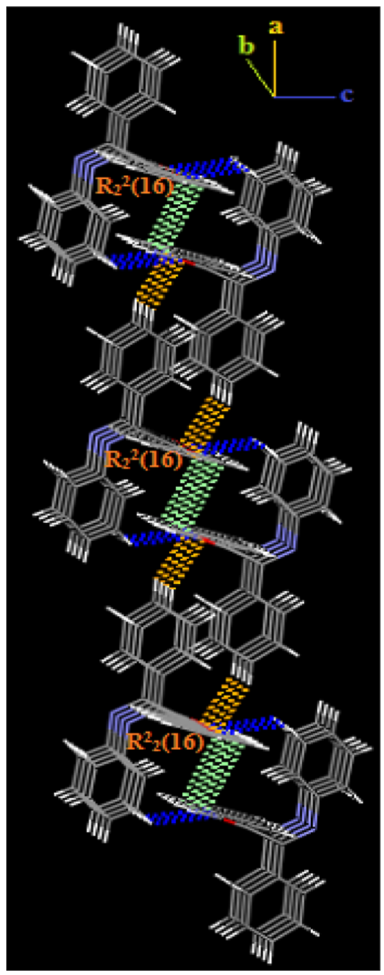

Figure 7. Intermolecular C12−H12···π(C5) interaction (orange) assisted vertical stacking of 1D hollow channels made up of $R_2^2(16)$ loops (bounded by blue lines representing the C17−H17···O1 hydrogen bonds and internally supported by the light green C3···C4 contacts) along the crystallographic *a* axis.

3.3.3. Imidorhenium Complex. In the domain of rhenium chemistry, the C−H···Cl interactions have been exploited as the ancillary H-bonds, mostly for the Re(I) complexes incorporating one Re^I−Cl bond derived from the $[Re^I(CO)_5Cl]$ precursor. Aiming to design the hitherto unknown self-associated supramolecular network tailored exclusively by the C−H···Cl H-bond interactions, we have opted for the *mer*-$[Re^V(NC_6H_5)Cl_3(PPh_3)_2]$ precursor over the well-explored $[Re^I(CO)_5Cl]$ complex due to the following reasons: (i) to maximize the number of electronically different metal-bound Cl atoms; (ii) to reduce polarizability of the Re^V-coordinated chlorine atoms, which can subsequently passivate their ability to act as the bifurcated H-bond acceptors; (iii) to eradicate free terminal oxygen atoms, unlike in $[Re^I(CO)_5Cl]$, in order to arrest the C−H···O interactions completely; (iv) to include an arene group in the precursor to insist intermolecular C−H···π interactions for additional stability and concomitant increase in dimensionality during self-assembly; and (v) to favor intramolecular $\pi-\pi$ interaction between the phenylimido

https://doi.org/10.1021/acsomega.4c07702
ACS Omega 2024, 9, 45518−45536

motif of the precursor and the C═N(Ph) group of the α-ketoimine ligand.

This strategic approach did not disappoint us. The crystal lattice of the imidorhenium complex exhibits a multitude of noncovalent intermolecular interactions, viz., C···C and C···Cl contacts, C−H···π interactions, and more importantly, the C−H···Cl hydrogen bonds, to boost a self-associated 3D supramolecular network. A centrosymmetric self-assembled dimer formed via the C14−H14···Cl3 hydrogen bonds (Figure 4g) is a noteworthy characteristic of molecular packing. Such a dimer creates the 14-member loop, $R_2^2(14)$, in which two metal centers are 7.3567(7) Å away. Polar C14···Cl3 nonbonded contact (Figure 4g) is an additional feature in the loops that provides supplementary support and stability. The loops are arranged in an eclipsing manner and mutually anchored by C18−H18···Cl2 H-bonds (Figure 4h) to create a 1D hollow tunnel that propagates along the crystallographic *a* axis. These 1D channels are found to remain interlinked sideways by the directional and satisfactorily linear C11−H11···π(C2) contacts [Figure 4i; 2.84(5) Å, 171(4)°] along the crystallographic *c* axis to generate a 2D pattern.

Along the *c* axis, adjacent centrosymmetric molecules of the two consecutive 1D channels are pairwise attached only by the attractive C11−H11···π(C2) force to form a different kind of $R_2^2(14)$ loop, in which two metal centers are 12.0943(8) Å away. Such $R_2^2(14)$ loops are interconnected through short edge-to-edge C12···C13 [Figure 4j, 3.222(7) Å] nonbonded contacts involving the phenyl groups of the N═C(Ph) motifs. A second type of C−H···π attractive force that draws our attention is the C6−H6···π(C26) interaction (Figure 4k, 2.86(3) Å, 158(3)°), occurring along the crystallographic *b* axis, which helps to stack the 2D patterns vertically to effectively create a 3D supramolecular network (Figure 8).

Intramolecular π−π stacking interaction also exists between the phenyl motifs (dihedral angle = 19.98°) of the Re(NPh) and C═N(Ph) groups (centroid−centroid distance is 3.775 Å). This may not have a direct effect on the intermolecular interactions; however, the spatial disposition of the respective phenyl moieties may subtly influence the overall molecular packing.

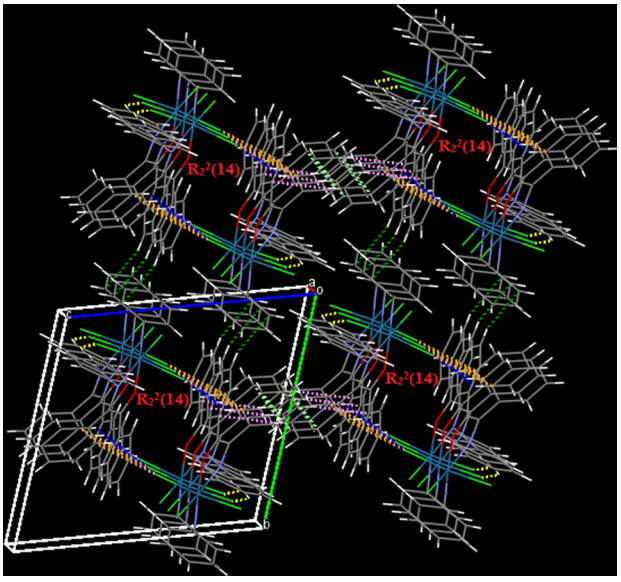

Figure 8. Self-assembled 3D supramolecular network of the imidorhenium complex. Color codes: C14−H14···Cl3, blue; C14···Cl3, orange; C18−H18···Cl2, yellow; C11−H11···π(C2), violet; C12···C13, light green; and C6−H6···π(C26), green.

3.4. Energy Decomposition Analysis. In order to delve into various physically meaningful energy components (permanent electrostatic, polarization, charge transfer, dispersion, and Pauli repulsion) associated with any noncovalent interaction, EDA in electronic structure theory is an indispensable analytical tool as it can quantify the forces of molecular association. Herein, we have chosen two nonvariational EDA methods of different theoretical origins to get critical insights into noncovalent interaction energy. To be specific, we have employed the natural bond orbital (NBO) based EDA (NEDA) structured on the antisymmetry of the intermediate wave functions, as well as, the symmetry-adapted perturbation theory (SAPT) based EDA that depends on perturbation to the Hamiltonian of the respective monomers.

3.5. Natural Energy Decomposition Analysis. Classical recognition of the chemical bonds and lone pairs on the basis of the Lewis concept[99] essentially forms the platform of natural bond orbital construction,[100] which has been implemented in the NEDA. Five-term DFT/NEDA interaction energy (ΔE_{NEDA}) can be partitioned into the electrostatic (ES), polarization (POL), charge transfer (CT), exchange−correlation (XC), and deformation (DEF) contributions ($\Delta E_{NEDA} = \Delta E_{ES} + \Delta E_{POL} + \Delta E_{CT} + \Delta E_{XC} + \Delta E_{DEF}$).[65]

Before proceeding to the interpretation of the NEDA results, it is instructive to briefly explain the origin of the energy components for a better understanding. ΔE_{ES} describes the permanent electrostatic interaction between the two unperturbed monomers prior to the supermolecule formation. ΔE_{POL} denotes the polarization interaction (electrostatic in origin) in a supermolecule arising from distortion of charge density of the individual monomers in presence of the other monomer in vicinity. ΔE_{XC} component is quantum mechanical in origin and imbibes the dual effects of electron exchange and electron correlation phenomena. The exchange stabilization between the electrons of the monomers arises as a consequence of the Pauli exclusion principle, and correlation energy originates from the instantaneous interactions between the electrons. Since London dispersion categorically stems from the electron correlation effect, the ΔE_{XC} component in NEDA inherently incorporates dispersion-borne stabilization if any.[101] However, compounding of the exchange and correlation effects in NEDA does not permit us to obtain the correlation energy exclusively. ΔE_{CT} accounts for the intermolecular electron delocalization interactions between the donor and acceptor orbitals of the two monomers in a supermolecule. In addition to the four aforesaid attractive interactions, ΔE_{DEF} is an intramolecular repulsive interaction that emerges from the distortion of the wave functions and electron density reorganization in the noninteracting monomers during the process of supermolecule formation.

From the NEDA data collected in Table 6, it is evident that the contributions of stabilizing energy components for any of the noncovalent interactions uniformly follow the order $\Delta E_{XC} > \Delta E_{POL} > \Delta E_{CT} > \Delta E_{ES}$. The undisputed predominance of ΔE_{XC} over the three other terms is implicative of a crucial role of electron correlation, i.e., the dispersion force. Although the two electron integrals between the occupied orbitals of the monomers in the dimer motifs given in Figure 4a−k are expected to be small, the cumulative effect of many such integrals can evolve as a strong dispersion component. A

https://doi.org/10.1021/acsomega.4c07702
ACS Omega 2024, 9, 45518−45536

Table 6. Five-Term NEDA Results (kcal/mol) Computed at the M06-2X-D3/def2-TZVP Level of Theory for the Existential Noncovalent Interactions in the Triad[a]

noncovalent interactions	referred figure	ΔE_{ES}	ΔE_{POL}	ΔE_{CT}	ΔE_{XC}	ΔE_{DEF}	ΔE_{NEDA}
C5−H5···O1	4a	−1.916 (18.3)	−3.030 (28.9)	−2.025 (19.3)	−3.520 (33.5)	7.482	−3.009
C7−H7···O1	4b	−4.913 (14.7)	−9.012 (26.9)	−7.024 (20.9)	−12.547 (37.5)	25.750	−7.746
C17−H17···O1	4c	−2.144 (10.1)	−7.084 (33.5)	−4.488 (21.2)	−7.433 (35.2)	17.359	−3.790
C5−H5···O1	4d	−2.346 (19.0)	−3.162 (25.6)	−2.564 (20.8)	−4.269 (34.6)	8.731	−3.610
C3···C4	4e	−6.438 (13.4)	−12.927 (26.9)	−8.639 (18.0)	−20.035 (41.7)	37.656	−10.383
C12−H12···π(C5)	BD of 4f	−1.599 (9.4)	−3.946 (23.1)	−4.111 (24.1)	−7.412 (43.4)	13.728	−3.340
$\pi_{(C9-C14)}-\pi_{(C9-C14)}$	AD of 4f	−2.666 (12.8)	−5.649 (27.1)	−3.642 (17.5)	−8.900 (42.6)	15.324	−5.533
C14−H14···Cl3	4g	−9.481 (13.2)	−22.835 (31.9)	−12.733 (17.8)	−26.508 (37.1)	55.530	−16.027
C18−H18···Cl2	4h	−3.670 (13.3)	−8.426 (30.6)	−4.973 (18.2)	−10.441 (37.9)	20.087	−7.423
C11−H11···π(C2)	4i	−2.878 (11.5)	−6.180 (24.6)	−4.765 (19.0)	−11.269 (44.9)	17.458	−7.634
C12···C13	4j	−4.365 (13.5)	−8.432 (26.0)	−5.775 (17.8)	−13.865 (42.7)	27.696	−4.741
C6−H6···π(C26)	4k	−2.011 (11.4)	−4.618 (26.1)	−3.622 (20.5)	−7.426 (42.0)	13.360	−4.317

[a]Values in the parentheses give the percentage contribution of that energy component to the total attractive energy originating from the XC, POL, CT, and ES components.

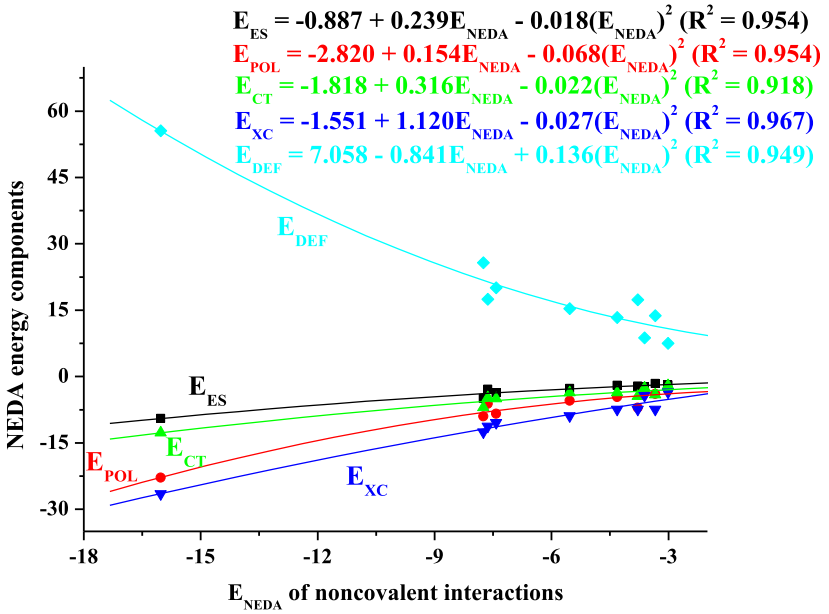

Figure 9. Variation of NEDA energy components (kcal/mol) with respect to the interaction energy of noncovalent interactions (kcal/mol) enlisted in Table 5 barring two C···C contacts.

scrutiny of the ΔE_{XC} percentage contributions (average) reveals that three types of noncovalent interactions, namely, C−H···π (43.4%), $\pi-\pi$ (42.6%), and C···C (42.2%), experience comparable exchange−correlation attraction, followed by C−H···Cl (37.5%) and least for the C−H···O (35.2%) interactions. The observed trend demonstrates that the dispersion force becomes less effective with the reduction in polarizability of the H-bond acceptors (π-electron > Cl > O). Since the dispersion energy is not directly afforded by NEDA, instead subsumed in the ΔE_{XC} values, we have also reported the SAPT results (vide infra) to resolve any ambiguity if lying with the quantification of the dispersion force.

NEDA results also manifest a striking observation that the contribution of ΔE_{POL} has been nearly doubled or even more, than the corresponding ΔE_{ES} component for each of the noncovalent interactions. It emphasizes that the attractive interaction between the induced multipoles of the monomers is far more significant than the attraction caused by the permanent charge separation. Lack of ionic charge separation in all the interactions is therefore partly responsible for the subdued role of permanent electrostatics.

NEDA further unfolds that the CT contributions for the enlisted interactions lie in between 17 to 25% of the total attractive force. The interfragment charge transfer process involves lp(O/Cl) → σ^*(C−H) electron delocalization for the C−H···O and C−H···Cl interactions, respectively. Such short-range charge transfer interactions are directional in nature and can likely play some determining role in orienting the molecular motifs to build the self-assembled network. The CT contributions appear to be somewhat favored by the enhanced ΔE_{POL} values, since polarization confers internal relaxation to the monomers facilitating a closer approach. Although the percentage contribution of CT may decline in reality owing to a general tendency of NEDA for overestimating the electron delocalization, the finite existence of CT in the reported noncovalent interactions cannot be ruled out.

At this point, it appears rational to investigate the dependence of NEDA-related energy components with respect

https://doi.org/10.1021/acsomega.4c07702
ACS Omega 2024, 9, 45518−45536

Table 7. Four-Term SAPT0 Results (kcal/mol) Computed at the SAPT0/jun-cc-pVDZ Level of Theory for All the Noncovalent Interactions in the Triad[a]

noncovalent interactions, graph set notation of supramolecular loop	referred figure	E_{elst}	E_{ex}	E_{ind}	E_{dis}	E_{SAPT0}
C5−H5···O1	4a	−2.11 (36.9)	1.74	−0.49 (8.6)	−3.12 (54.5)	−3.98
C7−H7···O1, $R_2^2(12)$	4b	−5.70 (32.3)	7.72	−1.17 (6.6)	−10.78 (61.1)	−9.93
C17−H17···O1, $R_2^2(16)$	4c	−2.29 (26.4)	3.70	−0.98 (11.3)	−5.41 (62.3)	−4.98
C5−H5···O1	4d	−2.47 (35.7)	2.24	−0.57 (8.3)	−3.87 (56.0)	−4.67
C3···C4	4e	−7.49 (30.2)	13.04	−1.72 (6.9)	−15.58 (62.8)	−11.75
C12−H12···π(C5)	BD of 4f	−1.80 (19.7)	4.95	−0.56 (6.1)	−6.79 (74.2)	−4.20
$\pi_{(C9-C14)}$−$\pi_{(C9-C14)}$	AD of 4f	−3.23 (27.3)	5.17	−0.82 (6.9)	−7.77 (65.7)	−6.65
C14−H14···Cl3, $R_2^2(14)$	4g	−15.44 (36.5)	16.35	−5.49 (12.9)	−21.39 (50.6)	−25.97
C18−H18···Cl2	4h	−2.76 (19.5)	5.54	−2.14 (15.2)	−9.22 (65.3)	−8.58
C11−H11···π(C2)	4i	−2.35 (16.8)	5.17	−1.12 (8.0)	−10.51 (75.2)	−8.81
C12···C13	4j	−4.59 (26.4)	11.85	−1.39 (8.0)	−11.40 (65.6)	−5.53
C6−H6···π(C26)	4k	−3.51 (29.7)	4.61	−1.06 (8.9)	−7.26 (61.4)	−7.22

[a]Values in the parentheses give the percentage contribution of that energy component to the total attractive energy emerging from the electrostatics, induction, and dispersion components.

to the interaction energy of the noncovalent interactions (barring the C···C contacts) that spans a range from −3 to −16 kcal/mol. The correlation results have been portrayed in Figure 9, which suggests that the energy terms bear acceptable quadratic relation (R^2 > 0.90 for each) with their respective interaction energies. All the lines diverge with the increase in ΔE_{NEDA}; however, the ΔE_{XC} and ΔE_{POL} lines steadily dip more than the ΔE_{CT} and ΔE_{ES} lines, particularly at higher ΔE_{NEDA} values.

Finally, the NEDA results attest that the exchange−correlation and polarization terms jointly share >65% of the total interaction energy. Modest contribution from charge transfer (∼20%) and even a lesser extent from electrostatics (<15%) have also been confirmed.

3.6. SAPT Analysis. The inadequacy of NEDA to quantify the dispersion energy has necessarily prompted us to undertake the SAPT analysis, which is the benchmark study in EDA. Moreover, in NEDA, the glimmering role of electrostatic component compared to polarization for all the noncovalent interactions warrants further checking, and the SAPT analysis is believed to clarify this aspect also.

Accuracy provided by the SAPT0 method with the truncated double-ζ basis set is trustworthy for most applications to get an elaborate description of noncovalent interaction energy (E_{SAPT0}) through partitioning into the electrostatic (E_{elst}), induction (E_{ind}), dispersion (E_{dis}), and exchange-repulsion (E_{ex}) components.[102] Among the four energy components, the first three components are attractive, and the last one is repulsive in nature. The SAPT0 results have been posted in Table 7.

The point, we wish to address first, is the varying degree of stabilization of the supramolecular building blocks, namely, $R_2^2(12)$, $R_2^2(16)$ and $R_2^2(14)$, observed in the α-diketone, α-ketoimine, and imidorhenium complex, respectively. The $R_2^2(12)$, $R_2^2(16)$ loops formed by C−H···O interactions experience −9.93 and −4.98 kcal/mol stabilization energy, respectively, and the $R_2^2(14)$ loop constructed by the C−H···Cl interactions encounters a stabilization of −25.97 kcal/mol [stability order: $R_2^2(14)$ > $R_2^2(12)$ > $R_2^2(16)$]. Substantial stabilization observed for the $R_2^2(14)$ loop is partly attributed to the short C···Cl polar contacts (Figure 4g) present concurrently with the C−H···Cl bonds. The electrostatic contribution is therefore expected to be on a higher side, and indeed it appears to be 36.5% of the total attractive energy. Increased electrostatic contribution (32.3%) existing in the $R_2^2(12)$ loop plausibly stems from the π−σ attraction occurring between the two tilted phenyl groups (Figure 4b). Unlike the above two, the $R_2^2(16)$ loop does not host any other subsidiary interaction except the C−H···O bonds, and decreased polarity of the C−H bonds has been reflected in a relatively lower electrostatic contribution (26.4%).

Another intriguing point of focus is the relative strength of the C−H···O interactions. Being consistent with Figure 4b, E_{SAPT0} for the $R_2^2(12)$ motif includes the energy of two C−H···O and one π−π stacking interactions. With an assumption of weak π−π interaction, E_{SAPT0} for the $R_2^2(12)$ motif can be therefore considered equivalent to two C7−H7···O1 interaction energies. Taking the two C7−H7···O1 (Figure 4b) and another C5−H5···O1 (Figure 4a) H-bond interactions, the average E_{SAPT0} for the three C−H···O interactions in the α-diketone becomes −4.63 kcal/mol. In a similar way, considering three C−H···O interactions related to Figure 4c (two C17−H17···O1) and 4d (one C5−H5···O1), the average E_{SAPT0} for the C−H···O interactions in the α-ketoimine appears to be −3.21 kcal/mol. Therefore, the average strength of the C−H···O bonds declines in the α-ketoimine compared to its α-diketone precursor, and this may necessitate the establishment of other noncovalent interactions to compensate for the loss in H-bond energy. Indeed, the C3···C4 contact (Figure 4e), C12−H12···π(C5) interaction (BD pair in Figure 4f), and π−π stacking (AD pair in Figure 4f) exist in the α-ketoimine lattice. All the moderately strong interactions are primarily nourished by the long-range dispersion force, and the permanent electrostatic force plays an assistive role in making a joint contribution of >90% to the interaction energy. We can now rank the noncovalent interactions in order of their strength to get an impression of their collaborative impact in the α-ketoimine: π−π (−6.65 kcal/mol) > C3···C4 (−5.87 kcal/mol) > C5−H5···O1 (−4.67 kcal/mol) > C12−H12···π(C5) (−4.20 kcal/mol) > C17−H17···O1 (−2.49 kcal/mol).

The C−H···Cl bonds in the imidorhenium complex experience ca. 85% of their interaction energy originating from the long-range dispersion and electrostatic forces. The average contribution of induction energy in the C−H···Cl bonds is higher than that in the C−H···O bonds due to the increase in polarizability of the Cl atoms, which in turn favors both the polarization and charge transfer interactions. Ancillary

https://doi.org/10.1021/acsomega.4c07702
ACS Omega 2024, 9, 45518−45536

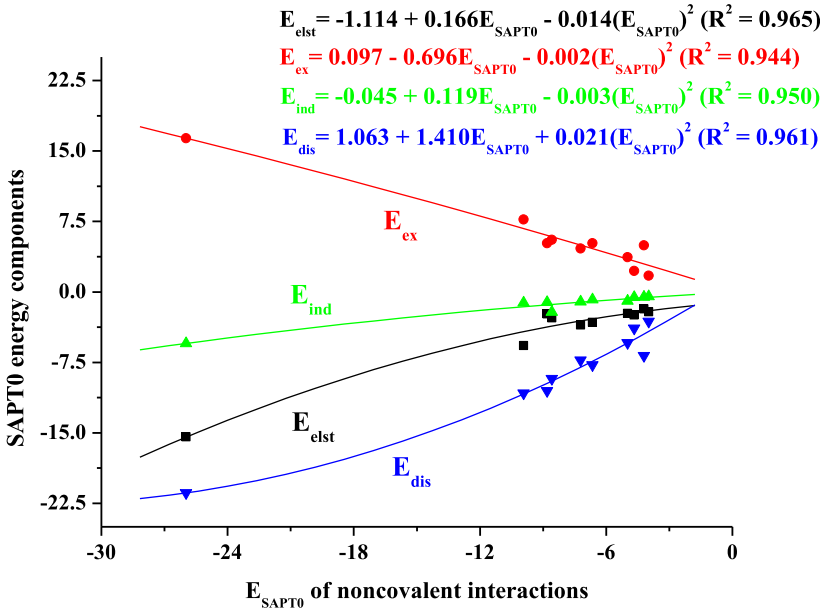

Figure 10. Variation of four SAPT0 energy components (kcal/mol) with respect to the interaction energy of noncovalent interactions (E_{SAPT0}, kcal/mol) enlisted in Table 7 barring the two C···C contacts.

non-tenuous interactions (C11−H11···π(C2), C6−H6···π-(C26), and C12···C13) in the complex show consistent domination of dispersion. It is worthy to note that, with the increase in linearity of the C11−H11···π(C2) interaction by 13° over the C6−H6···π(C26) contact, the percentage contribution of dispersion is enhanced by ∼14% in the former accompanied by a depletion in electrostatic contribution to a nearly same extent. This revelation clarifies that the degree of linearity in the C−H···π interactions chiefly decides its strength (Table 7).

Like in the NEDA section, here also, we have analyzed the variation of four SAPT0 energy components with respect to E_{SAPT0} (−4 to −26 kcal/mol) of the noncovalent interactions barring the C···C contacts. The interrelationship patterns (Figure 10) reflect that the four fundamental SAPT0 energy terms obey second-order polynomial dependence with the SAPT0 interaction energy. The leading coefficients for the E_{ex} and E_{ind} lines are quite small, and the polynomial regressions effectively transform into linear equations for those non-covalent interactions featured by E_{SAPT0} < 10 kcal/mol. Contrary to NEDA, where, variation of dispersion energy is mostly obscured in the ΔE_{XC} component, SAPT0 distinctly unravels the crucial roles of dispersion and permanent electrostatics in the context of C−H···O and C−H···Cl H-bonds.

3.7. Correlation of NEDA and SAPT Results. In the preceding sections, we have analyzed the energetics of noncovalent interactions by using two well-acclaimed EDA methods structured on independent decomposition and compounding of energy components. While SAPT directly affords dispersion energy, NEDA handles the dispersion force in the form of correlation effect through the ΔE_{XC} component. Again, NEDA furnishes both the polarization and charge transfer energy separately, whereas both the interactions are merged into induction energy in SAPT. Therefore, correlation studies (Figure 11a−d) between the energy components computed by NEDA and SAPT approaches can illuminate us regarding the effectiveness of the two methods.

Figure 11a reveals that the magnitudes of interaction energy of the noncovalent interactions computed by NEDA are uniformly less than their corresponding SAPT0 values. However, the E_{SAPT0} and E_{NEDA} values hold a satisfactorily acceptable linear relation with a coefficient of determination (R^2) of 0.958. Small departures have been noted at higher interaction energy; however, data points at lower energy nicely adhere to the regression line. Excellent linear correlation has been observed between the exchange−correlation energy computed by NEDA and the dispersion energy obtained from the SAPT0 method (Figure 11b, R^2 = 0.987). All the points cling to the regression line, and one can construe that the NEDA-derived exchange−correlation energy values are capable of statistically predicting the dispersion energy of the SAPT0 method at least in our triad. The data points in Figure 11c are a little scattered around the central line, although a fair linear regression exists (R^2 = 0.927). The observed scattering may arise from a compounding effect of polarization and charge transfer (induction energy) in SAPT, and also from a meager provision of charge transfer (in SAPT) that underestimates the NEDA-derived charge transfer. The correlation plot of permanent electrostatic energy (Figure 11d) also exhibits some deviation of points around the fitted line; however, linearity in regression analysis is retained (R^2 = 0.934). In conclusion, both the NEDA and SAPT0 results are individually robust, numerically stable, and produce interpretable solutions of their own.

3.8. QTAIM Analysis. QTAIM-derived electron density (ρ) at the bond critical point (BCP), ρ_{BCP}, of a covalent/noncovalent interaction is one of the reliable quantum observables, which can substantiate the electronic aspects of chemical bonding at the atomic level in real space. All the noncovalent interactions in the triad consistently manifest substantially low ρ_{BCP} values (<0.01 au, Table 8) at the (3, −1) critical points along the bond paths. Although the topological property of $\rho(r)$ is primarily regulated by the electron−nucleus force,[103] the topological property of its Laplacian ($\nabla^2\rho(r)$) depicts either a charge concentration or a charge depletion.[104]

https://doi.org/10.1021/acsomega.4c07702
ACS Omega 2024, 9, 45518−45536

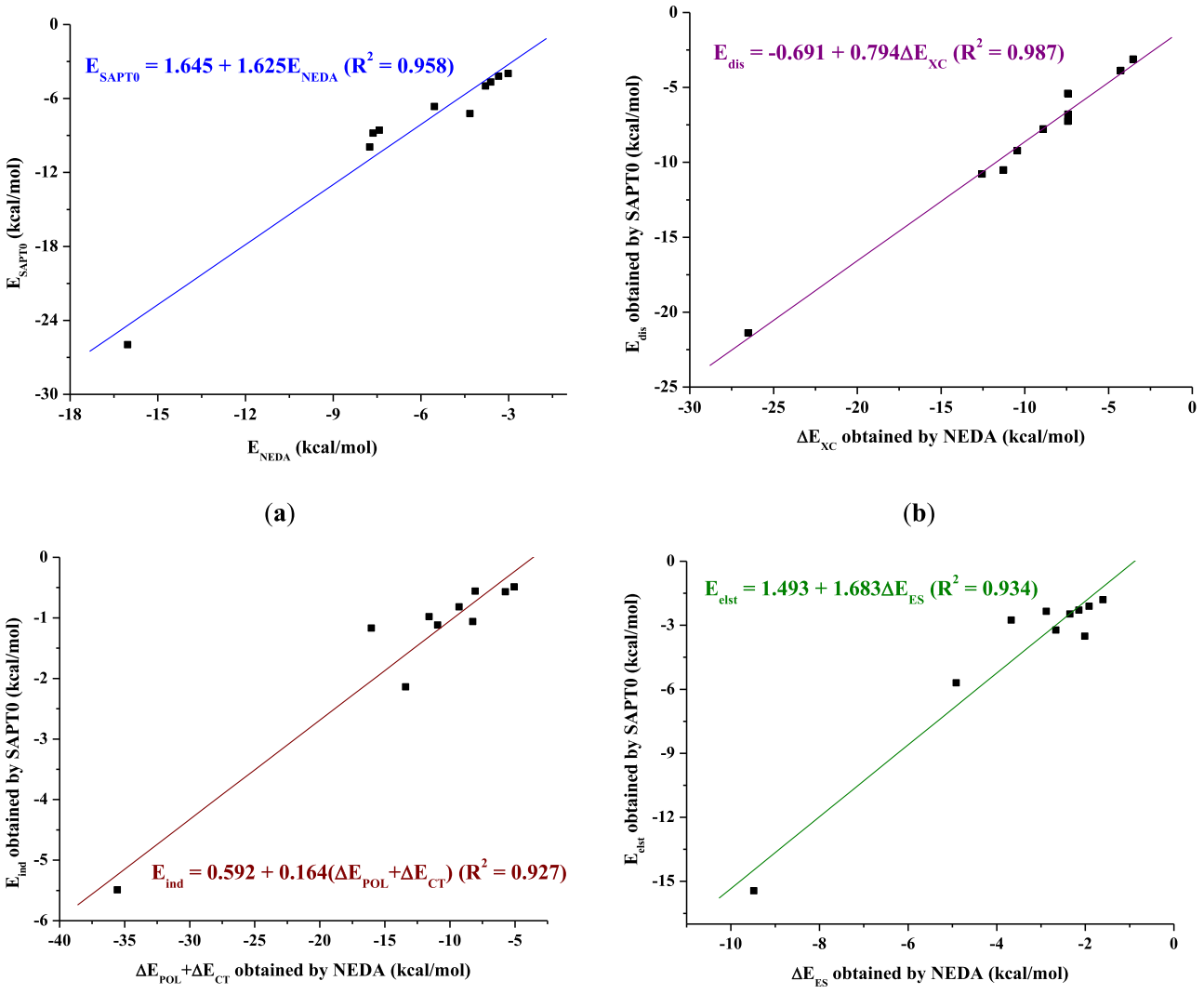

Figure 11. Correlation plots between various SAPT0 and NEDA energy components: (a) E_{SAPT0} and E_{NEDA}, (b) E_{dis} and ΔE_{XC}, (c) E_{ind} and ΔE_{POL} + ΔE_{CT}, and (d) E_{elst} and E_{ES}. All the noncovalent interactions enlisted in Table 5 have been considered except the two C···C contacts.

Electron density is considered to be reinforced at a BCP when $\nabla^2\rho_{BCP} < 0$, and a depletion is hinted by the condition $\nabla^2\rho_{BCP} > 0$.[105] The $\nabla^2\rho_{BCP}$ values ($0.006 < \nabla^2\rho_{BCP} < 0.033$) in Table 8 for the C−H···O, C−H···Cl, C−H···π, π−π, C···C, and C···Cl contacts are small positive quantities and imply that these interactions are purely noncovalent in nature.[106] To categorize any noncovalent interaction into closed-shell, intermediate, and covalent types, the ratio of two energy density parameters, specifically the $|V(r)|/G(r)$ index, has been advocated for reliable use.[107] All the noncovalent interactions in the triad can be classified as the closed-shell interactions due to fulfillment of the required condition, $|V(r)|/G(r) < 1$.

In common perspective, with the increased separation between two interacting atoms, electron density at the BCP of an interaction should decrease, and the bond loses its strength. Therefore, variation of ρ_{BCP} as a function of distance seems justified to systematically probe the changes in electron density between the interacting centers.[108] A correlation analysis between the ρ_{BCP} values and the bond lengths of some selected covalent and all the noncovalent interactions (Table 8) in the structurally characterized triad has been done. This correlation study is upper-bound at the sturdy covalent bonds (C═O and C═N), and the lowest limit has been set by the noncovalent interactions spanning a bond length range of 1.2−3.9 Å. From Figure 12, it can be unambiguously inferred that an increase in distance causes a drop in ρ_{BCP} following the first-order exponential decay expression, $y = 8.1043e^{-x/0.4095}$, having a very high coefficient of determination value of 0.997.

We have also searched for another interesting correlation between the ρ_{BCP} values and SAPT0/NEDA energy components. However, no admissible relation has emerged from the correlation study since the data points are irregularly scattered and do not fit in accordance with any valid mathematical function. This revelation affirms that the distances of noncovalent interactions in the lattices are internally governed by the individual packing patterns, and this packing effect in the solid state always remains unaccounted in the computation process. Hence, in this triad, computed electron densities at the BCPs of noncovalent

https://doi.org/10.1021/acsomega.4c07702
ACS Omega 2024, 9, 45518−45536

Table 8. QTAIM Descriptors (Computed at the M06-2X-D3/def2-TZVP Level) at the BCPs of the 14 Intermolecular Noncovalent Interactions and 5 Ligand-Based Covalent Bonds Found in the Triad

noncovalent interactions	d (Å)	$\rho(r)$ (a.u.)	$\nabla^2\rho(r)$ (a.u.)	$V(r)$ (a.u.)	$G(r)$ (a.u.)	$\lvert V(r)\rvert/G(r)$	$H(r)$ (a.u.)
C5−H5···O1 (α-diketone)	2.55(3)	0.0068	0.0277	−0.0041	0.0055	0.745	1.42×10^{-3}
C7−H7···O1 (α-diketone)	2.49(1)	0.0080	0.0322	−0.0048	0.0065	0.738	1.59×10^{-3}
$\pi_{(C2-C7)}$−$\pi_{(C2-C7)}$ (α-diketone)	3.848	0.0013	0.0063	−0.0007	0.0011	0.636	4.32×10^{-4}
C17−H17···O1 (α-ketoimine)	2.56(2)	0.0071	0.0308	−0.0044	0.0061	0.721	1.63×10^{-3}
C5−H5···O1 (α-ketoimine)	2.46(2)	0.0084	0.0327	−0.0047	0.0064	0.783	1.75×10^{-3}
C3···C4 (α-ketoimine)	3.343(2)	0.0066	0.0194	−0.0032	0.0040	0.775	8.23×10^{-4}
C12−H12···π(C5) (α-ketoimine)	2.80(2)	0.0057	0.0182	−0.0029	0.0038	0.763	7.91×10^{-4}
$\pi_{(C9-C14)}$−$\pi_{(C9-C14)}$ (α-ketoimine)	3.894	0.0039	0.0131	−0.0018	0.0025	0.720	7.43×10^{-4}
C14−H14···Cl3 (complex)	2.79(4)	0.0089	0.0325	−0.0050	0.0065	0.769	1.55×10^{-3}
C14···Cl3 (complex)	3.293(4)	0.0059	0.0192	−0.0029	0.0039	0.743	9.46×10^{-4}
C18−H18···Cl2 (complex)	2.87(5)	0.0065	0.0226	−0.0034	0.0045	0.755	1.12×10^{-3}
C11−H11···π(C2) (complex)	2.84(5)	0.0056	0.0178	−0.0029	0.0036	0.805	7.86×10^{-4}
C12···C13 (complex)	3.222(7)	0.0075	0.0219	−0.0038	0.0047	0.808	8.17×10^{-4}
C6−H6···π(C26) (complex)	2.86(3)	0.0054	0.0171	−0.0027	0.0035	0.771	7.68×10^{-4}
covalent interactions	d (Å)	$\rho(r)$ (a.u.)	$\nabla^2\rho(r)$ (a.u.)	$V(r)$ (a.u.)	$G(r)$ (a.u.)	$\lvert V(r)\rvert/G(r)$	$H(r)$ (a.u.)
C1−O1 (α-diketone)	1.214(2)	0.4076	0.1595	−1.4675	0.7537	1.947	-7.14×10^{-1}
C1−O1 (α-ketoimine)	1.215(2)	0.4069	0.1411	−1.4611	0.7482	1.953	-7.13×10^{-1}
C1−O1 (complex)	1.285(6)	0.3459	−0.1723	−1.1070	0.5320	2.081	-5.75×10^{-1}
C8−N1 (α-ketoimine)	1.275(2)	0.3781	−0.8388	−1.1013	0.4458	2.470	-6.55×10^{-1}
C8−N1 (complex)	1.340(7)	0.3272	−0.7755	−0.8417	0.3239	2.615	-5.18×10^{-1}

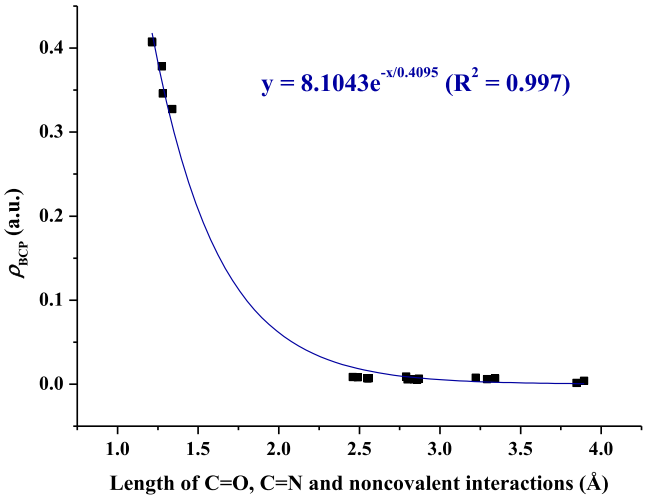

Figure 12. First-order exponential decay relationship between the ρ_{BCP} values computed at the M06-2X-D3/def2-TZVP level of theory and the crystallographically characterized distances of the noncovalent and covalent interactions collected in Table 8.

interactions are ineffectual to afford a satisfactory measure of the interaction energy.

3.9. IBSI Analysis. Lack of extrapolative nature between the ρ_{BCP} values and the SAPT0/NEDA energy components strongly indicates that the interaction energy is largely intrinsic to the lattice packing.[109] Originating from the independent gradient model (IGM),[110] the intrinsic bond strength index (IBSI)[70] can serve as an alternative to probe the strength of an interaction from the accumulated electron density between two selected atoms in any molecular environment. Since IBSI depends on the local stretching bond force constant, it can evaluate the inherent nature and strength of a bonding interaction, enabling a quantitative discrimination between the covalent (4.0 > IBSI > 0.15) and noncovalent interactions (0 < IBSI < 0.15).[70] The IBSI values of four C−H···O, two C−H···Cl, and three C−H···π interactions are presented in Table 9, and a mere inspection asserts noncovalent nature to these intermolecular interactions.

Table 9. IBSI, Δg^{pair}, and ρ_{BCP} Values Computed at the M06-2X-D3/def2-TZVP Level of Theory for the Four C−H···O, Two C−H···Cl, and Three C−H···π Interactions Found in the Triad

noncovalent interactions	d (Å)	ρ_{BCP} (a.u.)	Δg^{pair} (a.u.)	IBSI
C5−H5···O1 (α-diketone)	2.55(3)	0.0068	0.02810	0.00860
C7−H7···O1 (α-diketone)	2.49(1)	0.0080	0.03203	0.01033
C17−H17···O1 (α-ketoimine)	2.56(2)	0.0071	0.02842	0.00870
C5−H5···O1 (α-ketoimine)	2.46(2)	0.0084	0.03448	0.01132
C12−H12···π(C5) (α-ketoimine)	2.80(2)	0.0057	0.01803	0.00460
C14−H14···Cl3 (complex)	2.79(4)	0.0089	0.03878	0.00999
C18−H18···Cl2 (complex)	2.87(5)	0.0065	0.03641	0.00880
C11−H11···π(C2) (complex)	2.84(5)	0.0056	0.02222	0.00549
C6−H6···π(C26) (complex)	2.86(3)	0.0054	0.02023	0.00495

We have examined the relationship between the IBSI and the ρ_{BCP} parameters for a set of closed-shell H-bond interactions given in Table 9. Two aforementioned indices are interrelated via a quadratic regression equation, IBSI = $-0.036 + 10.936\rho_{BCP} - 646.984(\rho_{BCP})^2$, with $R^2 = 0.934$, and the corresponding parabolic curve has been depicted in Figure 13. Although IBSI is satisfactorily connected with ρ_{BCP} as revealed by the acceptable R^2 value, a modest scattering of the data points has been observed around the fitted curve. This deviation is attributed to the fact that the bulk of stabilization stems from the long-range force (dispersion and electrostatic) for the noncovalent interactions, and only a lesser amount arises from electron sharing.

A successful correlation of IBSI (physically linked to bond strength) with the ρ_{BCP} can shed valuable insights into the electronic effects exerted by intrinsic packing. However, it

https://doi.org/10.1021/acsomega.4c07702
ACS Omega 2024, 9, 45518−45536

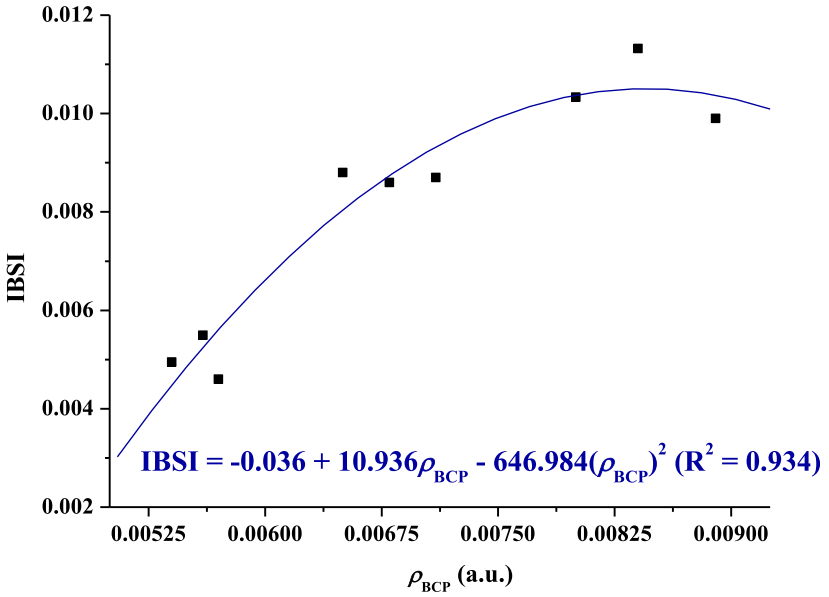

Figure 13. Quadratic regression curve correlating IBSI and ρ_{BCP} for the four C−H···O, two C−H···Cl, and three C−H···π interactions present in the triad.

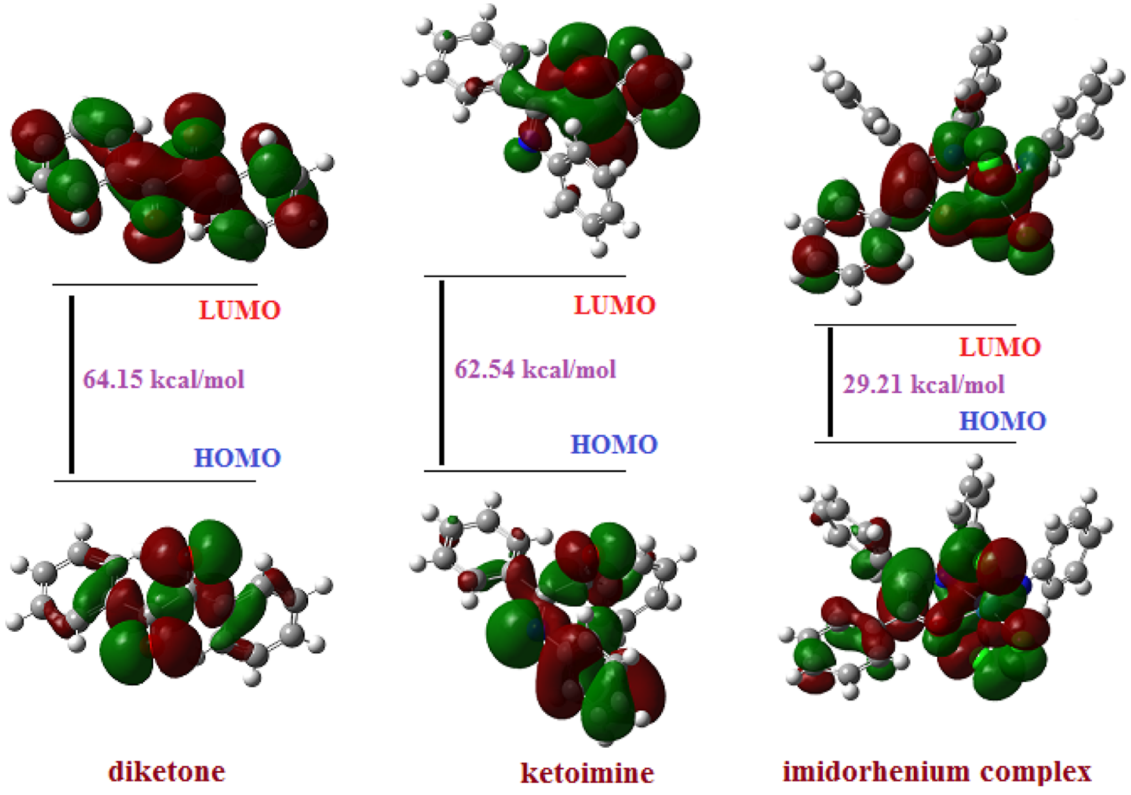

Figure 14. FMO energy analysis in the triad at M06L/def2-TZVP level of theory.

should be kept in mind that the success of interrelating IBSI with ρ_{BCP} as evolved from this study is indicative only and may not sustain in other cases.

3.10. Frontier Molecular Orbital (FMO) Analysis. FMO analysis is the *sine qua non* to trace the energy and composition of the HOMO and LUMO of any chemical compound, that can eventually probe the electron-rich and electron-deficient atomic centers inside the molecule. Evidently, the HOMO−LUMO energy differences are much comparable (<2 kcal/mol) for the α-diketone and α-ketoimine species (Figure 14). Upon α-ketoimine chelation to the Re^V center, the HOMO−LUMO energy difference in the complex has been drastically reduced to even less than the half of the HOMO−LUMO energy difference of free α-ketoimine. Huge depletion in the HOMO−LUMO energy gap by ca. 30 kcal/mol indicates an enhancement in polarizability of the imidorhenium species. Appreciable localization of the HOMO (>61%) over the *mer*-$ReCl_3$ moiety is again a testament to the markedly enhanced polarizability of the complex, which seems conducive for the Cl atoms to participate in the C−H···Cl bond formation.

https://doi.org/10.1021/acsomega.4c07702
ACS Omega 2024, 9, 45518−45536

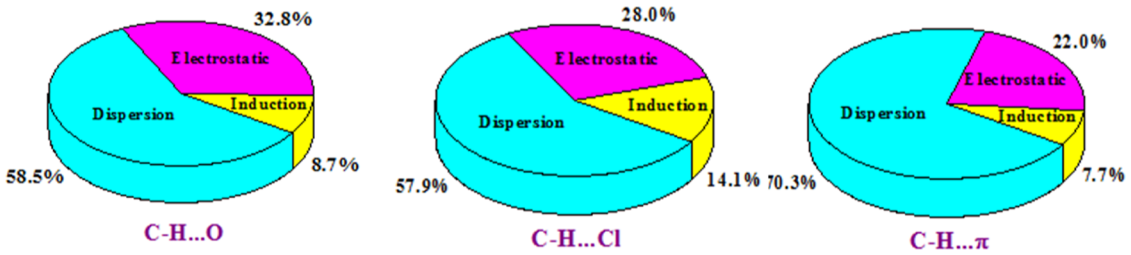

Figure 15. Pie charts showing the average contributions of the SAPT0 energy components for the C−H···O (left), C−H···Cl (middle), and C−H···π (right) interactions present in the triad.

4. CONCLUSIONS

The present work has unfurled the exquisite roles of traditionally feeble C−H···O and C−H···Cl hydrogen bonds toward stabilizing the 2D and 3D molecular frameworks in the triad. The inescapable conclusions emerging from our study are enumerated below.

(i) The 2D molecular network in benzil is not purely governed by the van der Waals force as earlier suggested by Brown and Sadanaga. Instead, moderately strong C−H···O bonds, being accompanied by the $\pi-\pi$ interaction, play an obligatory role in molecular packing.

(ii) Intramolecular N···H interaction obfuscates any further possibility of intermolecular C−H···N interaction in the α-ketoimine. Consequently, 2D self-assembled molecular packing in the α-ketoimine is dictated by the C−H···O hydrogen bonds, and strategic functionalization/substitution at the imine backbone can influence the dimensionality of packing in other benzil-based ketoimine species.

(iii) In rhenium chemistry, hitherto unknown 3D self-assembled supramolecular architecture constructed only by the C−H···Cl hydrogen bonds has now been unraveled with this imidorhenium complex. Search for other fascinating architectures by exploring even weaker C−H···Br interactions is currently underway using different $[Re(NC_6H_4Y)Br_3(PPh_3)_2]$ precursors (Y═H, CH_3, Cl, Br, and OCH_3).

(iv) Average contributions of the dispersion, electrostatic, and induction forces are 58.5, 32.8, and 8.7%, respectively, for the four intermolecular C−H···O interactions observed in the two organics. The C−H···Cl interactions found in the imidorhenium complex experience comparable contribution from the dispersion force, i.e., 57.9% on average. However, the electrostatic and induction forces contribute 28.0 and 14.1%, respectively, on average. For the C−H···π interactions, dispersion force contributes to the highest extent, reaching up to 70.3%, followed by the electrostatic (22.0%) and least for the induction component (7.7%). Average contributions of three different stabilizing energy components related to the C−H···O, C−H···Cl, and C−H···π interactions are depicted in the circular statistical graphics for a quick look (Figure 15).

(v) Since SAPT0 and NEDA energy components do not hold any satisfactory linear relationship with ρ_{BCP}, the electron density existing between the donor and acceptor atoms of a noncovalent interaction in the triad is primarily regulated by the crystal-specific intrinsic packing instead of the chemical nature of the H-bond donors and acceptors.

(vi) FMO analysis suggests that a significant HOMO−LUMO energy reduction in the imidorhenium complex and a considerable localization of electron density over the Re^V-bound Cl atoms indeed ameliorate the C−H···Cl bond formation.

■ ASSOCIATED CONTENT

Supporting Information

The Supporting Information is available free of charge at https://pubs.acs.org/doi/10.1021/acsomega.4c07702.

Olex2−1.5-derived Cartesian coordinates for all the noncovalent interactions observed in the α-diketone, α-ketoimine, and imidorhenium complex; Cartesian coordinates and total energy of the optimized α-diketone, α-ketoimine, and imidorhenium complex in the gas phase at the M06L/def2-TZVP level of theory; IR spectra of the α-ketoimine and imidorhenium complex; and 500 MHz ^{1}H NMR spectra of the α-ketoimine and imidorhenium complex (PDF)

α-Diketone data (CIF)

α-Ketoimine data (CIF)

Imidorhenium complex data (CIF)

■ AUTHOR INFORMATION

Corresponding Authors

Suparna Banerjee − *Department of Chemistry, Uluberia College, University of Calcutta, Howrah 711315, India;* orcid.org/0009-0000-6339-093X; Email: suparnaban@rediffmail.com

Jaydip Gangopadhyay − *Department of Chemistry, St. Paul's Cathedral Mission College, University of Calcutta, Kolkata 700009, India;* orcid.org/0000-0003-2328-2701; Email: gjaydip@rediffmail.com

Authors

Ankita Sinha − *Department of Chemistry, St. Paul's Cathedral Mission College, University of Calcutta, Kolkata 700009, India;* orcid.org/0009-0002-4165-242X

Suphal Sen − *School of Applied Material Sciences, Central University of Gujarat, Gandhinagar 382030 Gujarat, India*

Tejender Singh − *Tata Institute of Fundamental Research, Hyderabad 500046, India*

Aniruddha Ghosh − *Department of Chemistry, St. Paul's Cathedral Mission College, University of Calcutta, Kolkata 700009, India*

Satyen Saha − *Department of Chemistry, Institute of Science, Banaras Hindu University, Varanasi 221005 Uttar Pradesh, India;* orcid.org/0000-0001-6915-9384

https://doi.org/10.1021/acsomega.4c07702
ACS Omega 2024, 9, 45518−45536

Krishanu Bandyopadhyay − *Department of Chemistry, Institute of Science, Banaras Hindu University, Varanasi 221005 Uttar Pradesh, India*
Arindam Dey − *Department of Chemistry, Scottish Church College, University of Calcutta, Kolkata 700006, India*

Complete contact information is available at: https://pubs.acs.org/10.1021/acsomega.4c07702

Notes

The authors declare no competing financial interest.

■ ACKNOWLEDGMENTS

Since no external funding has been received to carry out this research, J.G. and S.B. have defrayed the expenses to purchase the chemicals and other essentials. We sincerely thank St. Paul's Cathedral Mission College, Kolkata, for providing the essential infrastructural facilities to pursue the research work. As always, J.G. expresses his gratitude to Swami Divyananda Maharaj, Ex-Principal of RKMVCC, Kolkata, and Prof. Amalesh Banerjee, Ex-HOD of Economics of Rabindra Bharati University, Kolkata, for their unwavering support in many ways. J.G. gratifyingly admires the coaxing of his daughter Adrija.

■ REFERENCES

(1) Scheiner, S. Understanding noncovalent bonds and their controlling forces. *J. Chem. Phys.* **2020**, *153*, 140901.
(2) Nishio, M. CH/π hydrogen bonds in crystals. *CrystEngComm* **2004**, *6* (27), 130−158.
(3) Nishio, M.; Umezawa, Y.; Honda, K.; Tsuboyama, S.; Suezawa, H. CH/π hydrogen bonds in organic and organometallic chemistry. *CrystEngComm* **2009**, *11*, 1757.
(4) Watt, M. M.; Collins, M. S.; Johnson, D. W. Ion-π Interactions in Ligand Design for Anions and Main Group Cations. *Acc. Chem. Res.* **2013**, *46* (4), 955−966.
(5) Dougherty, D. A. The Cation-π Interaction. *Acc. Chem. Res.* **2013**, *46* (4), 885−893.
(6) Ma, J. C.; Dougherty, D. A. The Cation-π Interaction. *Chem. Rev.* **1997**, *97* (5), 1303−1324.
(7) Fujisawa, K.; Humbert-Droz, M.; Letrun, R.; Vauthey, E.; Wesolowski, T. A.; Sakai, N.; Matile, S. Ion Pair-π Interactions. *J. Am. Chem. Soc.* **2015**, *137* (34), 11047−11056.
(8) Mooibroek, T. J.; Gamez, P.; Reedijk, J. Lone pair-π interactions: a new supramolecular bond? *CrystEngComm* **2008**, *10*, 1501−1515.
(9) Egli, M.; Sarkhel, S. Lone Pair-Aromatic Interactions: To Stabilize or Not to Stabilize. *Acc. Chem. Res.* **2007**, *40* (3), 197−205.
(10) Janiak, C. A critical account on π-π stacking in metal complexes with aromatic nitrogen-containing ligands. *J. Chem. Soc., Dalton Trans.* **2000**, 3885−3896.
(11) Martinez, C. R.; Iverson, B. L. Rethinking the term "pi-stacking. *Chem. Sci.* **2012**, *3*, 2191−2201.
(12) Thakuria, R.; Nath, N. K.; Saha, B. K. The Nature and Applications of π-π Interactions: A Perspective. *Cryst. Growth Des.* **2019**, *19*, 523−528.
(13) Politzer, P.; Murray, J. S.; Clark, T. Halogen bonding and other σ-hole interactions: a perspective. *Phys. Chem. Chem. Phys.* **2013**, *15*, 11178−11189.
(14) Politzer, P.; Murray, J. S.; Clark, T.; Resnati, G. The σ-hole revisited. *Phys. Chem. Chem. Phys.* **2017**, *19*, 32166−32178.
(15) Politzer, P.; Murray, J. S. σ-Hole Interactions: Perspectives and Misconceptions. *Crystals* **2017**, *7* (7), 212.
(16) Wang, H.; Wang, W.; Jin, W. J. σ-Hole Bond vs π-Hole Bond: A Comparison Based on Halogen Bond. *Chem. Rev.* **2016**, *116* (9), 5072−5104.
(17) Politzer, P.; Murray, J. S.; Clark, T. The π-hole revisited. *Phys. Chem. Chem. Phys.* **2021**, *23*, 16458−16468.
(18) Scheiner, S. Dissection of the Origin of π-Holes and the Noncovalent Bonds in Which They Engage. *J. Phys. Chem. A* **2021**, *125* (30), 6514−6528.
(19) Scheiner, S. Anatomy of π-hole bonds: Linear systems. *J. Chem. Phys.* **2021**, *155*, 174302.
(20) Hubbard, R. E.; Kamran Haider, M. Hydrogen Bonds in Proteins: Role and Strength. *Encyclopedia of Life Sciences (ELS)*; John Wiley & Sons, Ltd: Chichester, 2010.
(21) Matienko, L. I.; Mil, E. M.; Albantova, A. A.; Goloshchapov, A. N. The Role H-Bonding and Supramolecular Structures in Homogeneous and Enzymatic Catalysis. *Int. J. Mol. Sci.* **2023**, *24* (23), 16874.
(22) Gerlt, J. A.; Kreevoy, M. M.; Cleland, W. W.; Frey, P. A. Understanding enzymic catalysis: the importance of short, strong hydrogen bonds. *Chem. Biol.* **1997**, *4*, 259−267.
(23) Olejnik, A.; Dec, B.; Goddard, W. A.; Bogdanowicz, R. Hopping or Tunneling? Tailoring the Electron Transport Mechanisms through Hydrogen Bonding Geometry in the Boron-Doped Diamond Molecular Junctions. *J. Phys. Chem. Lett.* **2022**, *13* (34), 7972−7979.
(24) Meot-Ner Mautner, M. The Ionic Hydrogen Bond. *Chem. Rev.* **2005**, *105* (1), 213−284.
(25) Ishikita, H.; Saito, K. Proton transfer reactions and hydrogen-bond networks in protein environments. *J. R. Soc. Interface* **2014**, *11* (91), 20130518.
(26) Zhang, Z.; Li, D.; Jiang, W.; Wang, Z. The electron density delocalization of hydrogen bond systems. *Adv. Phys.: X* **2018**, *3* (1), 1428915.
(27) Gellman, S. H. Introduction: Molecular Recognition. *Chem. Rev.* **1997**, *97* (5), 1231−1232.
(28) Brooijmans, N.; Kuntz, I. D. Molecular recognition and docking algorithms. *Annu. Rev. Biophys. Biomol. Struct.* **2003**, *32*, 335−373.
(29) Izatt, R. M.; Izatt, S. R.; Izatt, N. E.; Krakowiak, K. E.; Bruening, R. L.; Navarro, L. Industrial applications of molecular recognition technology to separations of platinum group metals and selective removal of metal impurities from process streams. *Green Chem.* **2015**, *17*, 2236−2245.
(30) Saenger, W.; Steiner, T. Cyclodextrin Inclusion Complexes: Host-Guest Interactions and Hydrogen-Bonding Networks. *Acta Crystallogr.* **1998**, *54*, 798−805.
(31) Wagner, B. D. Hydrogen bonding of excited states in supramolecular host−guest inclusion complexes. *Phys. Chem. Chem. Phys.* **2012**, *14*, 8825−8835.
(32) Liu, Y.; Jiang, Z.; Wang, L.; Cheng, Y.; Fan, W.; Bian, L.; Shi, Y.; Zheng, L. Y.; Cao, Q. E. Hydrogen Bond-Modulating Luminescent Properties of Organic Cocrystal Materials. *Cryst. Growth Des.* **2024**, *24* (1), 132−142.
(33) Gong, L. K.; Hu, Q. Q.; Huang, F. Q.; Zhang, Z. Z.; Shen, N. N.; Hu, B.; Song, Y.; Wang, Z. P.; Du, K. Z.; Huang, X. Y. Efficient modulation of photoluminescence by hydrogen bonding interactions between inorganic $[MnBr_4]^{2-}$ anions and organic cations. *Chem. Commun.* **2019**, *55*, 7303−7306.
(34) Liu, Y.; Wang, L.; Zhao, L.; Zhang, Y.; Li, Z. T.; Huang, F. Multiple hydrogen bonding driven supramolecular architectures and their biomedical applications. *Chem. Soc. Rev.* **2024**, *53*, 1592−1623.
(35) Lin, C.; Xiao, T.; Wang, L. *Hydrogen Bonded Supramolecular Structures*; Springer: Berlin, 2015.
(36) June Sutor, D. The C−H... O Hydrogen Bond in Crystals. *Nature* **1962**, *195*, 68−69.
(37) Sutor, D. J. 204. Evidence for the existence of C−H···O hydrogen bonds in crystals. *J. Chem. Soc.* **1963**, *0*, 1105−1110.
(38) Donohue, J.. In *Structural Chemistry and Molecular Biology*; Rich, A., Davidson, N., Eds.; W.H.Freeman & Co Ltd, 1968; . San Francisco, CA.
(39) Taylor, R.; Kennard, O. Crystallographic evidence for the existence of CH.cntdot.cntdot.cntdot.O, CH.cntdot.cntdot.cntdot.N and CH.cntdot.cntdot.cntdot.Cl hydrogen bonds. *J. Am. Chem. Soc.* **1982**, *104*, 5063−5070.

(40) Horowitz, S.; Trievel, R. C. Carbon-Oxygen hydrogen bonding in biological structure and function. *J. Biol. Chem.* **2012**, *287* (50), 41576−41582.
(41) Wahl, M. C.; Sundaralingam, M. C-H···O hydrogen bonding in biology. *Trends Biochem. Sci.* **1997**, *22* (3), 97−102.
(42) Derewenda, Z. S. C-H Groups as Donors in Hydrogen Bonds: A Historical Overview and Occurrence in Proteins and Nucleic Acids. *Int. J. Mol. Sci.* **2023**, *24* (17), 13165.
(43) Desiraju, G. R. The C-H···O Hydrogen Bond in Crystals: What is it? *Acc. Chem. Res.* **1991**, *24* (10), 290−296.
(44) Desiraju, G. R. The C-H···O Hydrogen Bond: Structural Implications and Supramolecular Design. *Acc. Chem. Res.* **1996**, *29*, 441−449.
(45) Desiraju, G. R. Supramolecular Synthons in Crystal Engineering-A New Organic Synthesis. *Angew. Chem., Int. Ed. Engl.* **1995**, *34*, 2311−2327.
(46) Aakeroy, C. B.; Evans, T. A.; Seddon, K. R.; Palinko, I. The C−H···Cl hydrogen bond: does it exist? *New J. Chem.* **1999**, *23*, 145−152.
(47) Aullon, G.; Bellamy, D.; Guy Orpen, A.; Brammer, L.; Bruton, E. A. Metal-bound chlorine often accepts hydrogen bonds. *Chem. Commun.* **1998**, 653−654.
(48) Jones, P. G.; Ahrens, B. Bis(diphenylphosphino)methane and related ligands as hydrogen bond donors. *Chem. Commun.* **1998**, 2307−2308.
(49) Navon, O.; Bernstein, J.; Khodorkovsky, V. Ketten, Leitern und Schichten durch Halogen-Halogen- und Halogen-Wasserstoff-Wechselwirkungen. *Angew. Chem.* **1997**, *109* (6), 640−642.
(50) Freytag, M.; Jones, P. G. Hydrogen bonds C−H··Cl as a structure-determining factor in the gold(i) complex bis(3-bromopyridine)gold(i) dichloroaurate(i). *Chem. Commun.* **2000**, 277−278.
(51) Chakraborty, I.; Panda, B. K.; Gangopadhyay, J.; Chakravorty, A. Rhenium chemistry of azooximes: oxygen atom transfer, azoimine chelation, and imine-oxime contrast. *Inorg. Chem.* **2005**, *44*, 1054−1060.
(52) Banerjee, S.; Bhattacharyya, S.; Dirghangi, B. K.; Menon, M.; Chakravorty, A. Chemistry of the Rhenium−Azopyridine Family: An Oxo Parent and Derivatives Thereof Including a Novel Oxo−Imido Dimer. *Inorg. Chem.* **2000**, *39*, 6−13.
(53) Das, S.; Chakraborty, I.; Chakravorty, A. Chemistry of azopyrimidine chelates of $Re^{V}O$, $Re^{III}OPPh_3$ and $Re^{V}NAr$. *Polyhedron* **2003**, *22*, 901−907.
(54) Das, S. Synthesis and characterization of new imidorhenium(V) and imidorhenium(VI) complexes of pyridyltriazines and pyrazinyltriazine with halide coligands including rare iodide. *Inorg. Chim. Acta* **2008**, *361*, 2815−2820.
(55) Gangopadhyay, J.; Banerjee, S.; Chen, J.-T.; Lu, C.-Z. Intramolecular amide→imine reduction in higher valent rhenium complexes stabilized by arylimido coligand: Rate studies and effect of reductants. *Polyhedron* **2009**, *28*, 2503−2509.
(56) Gangopadhyay, J.; Sengupta, S.; Bhattacharyya, S.; Chakraborty, I.; Chakravorty, A. Pyridylazole Chelation of Oxorhenium(V) and Imidorhenium(V). Rates and Trends of Oxygen Atom Transfer from $Re^{V}O$ to Tertiary Phosphines. *Inorg.Chem.* **2002**, *41*, 2616−2622.
(57) Gerber, T. I. A.; Luzipo, D.; Mayer, P. A rhenium(V) complex containing a terdentate chelate with an imido donor atom: synthesis and structure of $[Re(aps)I(PPh_3)_2]I$ (H_3aps = N-(2-aminophenyl)-salicylideneimine). *J. Coord. Chem.* **2006**, *59*, 1149−1155.
(58) Lohrey, T. D.; Cortes, E. A.; Bergman, R. G.; Arnold, J. Facile Activation of Triarylboranes by Rhenium(V) Oxo Imido Complexes. *Inorg. Chem.* **2020**, *59*, 7216−7226.
(59) Das, S.; Chakraborty, I.; Chakravorty, A. Rhenium Chemistry of Diazabutadienes and Derived Iminoacetamides Spanning the Valence Domain II−VI. Synthesis, Characterization, and Metal-Promoted Regiospecific Imine Oxidation. *Inorg. Chem.* **2003**, *42*, 6545−6555.
(60) Masui, C. S.; Mayer, J. M. Imido and amido complexes of hydrotris (pyrazolyl) borate-rhenium. *Inorg. Chim. Acta.* **1996**, *251*, 325−333.
(61) Dilworth, J. R.; Lewis, J. S.; Miller, J. R.; Zheng, Y. The preparation of rhenium (V) oxo and imido complexes with $Et_2NCSNHCOPh$ and $Et_2NCSBC(NH)Ph$. The x-ray crystal structure of $[ReOCl(PhCONCSNEt_2)_2]$. *Polyhedron* **1993**, *12*, 221−225.
(62) Wang, Y. P.; Che, C. M.; Wong, K. Y.; Peng, S. M. Spectroscopy, molecular structure, and electrochemistry of rhenium-(V) oxo and imido complexes of 1,4,8,11-tetraazacyclotetradecane (cyclam). *Inorg. Chem.* **1993**, *32*, 5827−5832.
(63) Alemayehu, A. B.; Teat, S. J.; Borisov, S. M.; Ghosh, A. Rhenium-imido corroles. *Inorg. Chem.* **2020**, *59*, 6382−6389.
(64) Glendening, E. D.; Streitwieser, A. Natural energy decomposition analysis: An energy partitioning procedure for molecular interactions with application to weak hydrogen bonding, strong ionic, and moderate donor−acceptor interactions. *J. Chem. Phys.* **1994**, *100*, 2900−2909.
(65) Glendening, E. D. Natural Energy Decomposition Analysis: Explicit Evaluation of Electrostatic and Polarization Effects with Application to Aqueous Clusters of Alkali Metal Cations and Neutrals. *J. Am. Chem. Soc.* **1996**, *118* (10), 2473−2482.
(66) Schenter, G. K.; Glendening, E. D. Natural Energy Decomposition Analysis: The Linear Response Electrical Self Energy. *J. Phys. Chem.* **1996**, *100* (43), 17152−17156.
(67) Jeziorski, B.; Moszynski, R.; Szalewicz, K. Perturbation theory approach to intermolecular potential energy surfaces of van der Waals complexes. *Chem. Rev.* **1994**, *94*, 1887−1930.
(68) Bader, R. F. W. *Atoms in Molecules, a Quantum Theory*; Oxford University Press: Oxford, UK, 1990.
(69) *Quantum Theory of Atoms in Molecules: recent Progress in Theory and Application*; Matta, C., Boyd, R. J., Eds.; Wiley-VCH Weinheim: Germany, 2007.
(70) Klein, J.; Khartabil, H.; Boisson, J.-C.; Contreras-García, J.; Piquemal, J.-P.; Hénon, E. New Way for Probing Bond Strength. *J. Phys. Chem. A* **2020**, *124*, 1850−1860.
(71) Parshall, G. W.; Shive, L. W.; Cotton, F. A. Phosphine Complexes of Rhenium. *Inorg. Synth.* **1977**, *17*, 110−111.
(72) Chatt, J.; Garforth, J. D.; Jhonson, N. P.; Rowe, G. A. Nitrido- and arylimido-complexes of rhenium. *J. Chem. Soc.* **1964**, 1012−1020.
(73) Sheldrick, G. M. SHELXT − Integrated space-group and crystal structure determination. *Acta Crystallogr.* **2015**, *71*, 3−8.
(74) Sheldrick, G. M. A short history of *SHELX*. *Acta Crystallogr.* **2008**, *64*, 112−122.
(75) Sheldrick, G. M. *SHELXL-2018*; Universität Göttingen: Göttingen, Germany, 2018.
(76) Sheldrick, G. M. *SHELXS-97, Program for Crystal Structure Solution*; University of Gottingen: Gottingen, Germany, 1997.
(77) Dolomanov, O. V.; Bourhis, L. J.; Gildea, R. J.; Howard, J. A. K.; Puschmann, H. OLEX2: a complete structure solution, refinement and analysis program. *J. Appl. Crystallogr.* **2009**, *42*, 339−341.
(78) Macrae, C. F.; Sovago, I.; Cottrell, S. J.; Galek, P. T. A.; McCabe, P.; Pidcock, E.; Platings, M.; Shields, G. P.; Stevens, J. S.; Towler, M.; Wood, P. A. *Mercury 4.0*: from visualization to analysis, design and prediction. *J. Appl. Crystallogr.* **2020**, *53*, 226−235.
(79) Frisch, M. J.; Trucks, G. W.; Schlegel, H. B.; Scuseria, G. E.; Robb, M. A.; Cheeseman, J. R.; Scalmani, G.; Barone, V.; Petersson, G. A.; Nakatsuji, H.; et al. *GAUSSIAN 16*. Revision C.01; Gaussian, Inc.: Wallingford CT, 2019.
(80) Zhao, Y.; Truhlar, D. G. The M06 suite of density functionals for main group thermochemistry, thermochemical kinetics, noncovalent interactions, excited states, and transition elements: two new functionals and systematic testing of four M06-class functionals and 12 other functionals. *Theor. Chem. Acc.* **2008**, *120*, 215−241.
(81) Zhao, Y.; Truhlar, D. G. Density Functionals with Broad Applicability in Chemistry. *Acc. Chem. Res.* **2008**, *41*, 157−167.
(82) Grimme, S.; Antony, J.; Ehrlich, S.; Krieg, H. A. A consistent and accurate *ab initio* parametrization of density functional dispersion

https://doi.org/10.1021/acsomega.4c07702
ACS Omega 2024, 9, 45518−45536

correction (DFT-D) for the 94 elements H-Pu. *J. Chem. Phys.* **2010**, *132* (15), 154104.
(83) Weigend, F.; Ahlrichs, R. Balanced basis sets of split valence, triple zeta valence and quadruple zeta valence quality for H to Rn: Design and assessment of accuracy. *Phys. Chem. Chem. Phys.* **2005**, *7*, 3297−3305.
(84) Gaussian. *GaussView 6.0*; Gaussian Inc.: Wallingford, CT, USA, 2017.
(85) Lu, T.; Chen, F. Multiwfn A multifunctional wavefunction analyzer. *J. Comput. Chem.* **2012**, *33*, 580−592.
(86) Dunning, T. H., Jr. Gaussian basis sets for use in correlated molecular calculations. I. The atoms boron through neon and hydrogen. *J. Chem. Phys.* **1989**, *90*, 1007−1023.
(87) Turney, J. M.; Simmonett, A. C.; Parrish, R. M.; Hohenstein, E. G.; Evangelista, F. A.; Fermann, J. T.; Mintz, B. J.; Burns, L. A.; Wilke, J. J.; Abrams, M. L.; et al. PSI4: An Open-Source Ab Initio Electronic Structure Program. *Wiley Interdiscip. Rev.: Comput. Mol. Sci.* **2012**, *2*, 556−565.
(88) Glendening, E. D.; Badenhoop, J. K.; Reed, A. E.; Carpenter, J. E.; Bohmann, J. A.; Morales, C. M.; Karafiloglou, P.; Landis, C. R.; Weinhold, F. *NBO 7.0*; Theoretical Chemistry Institute; University of Wisconsin: Madison, WI, 2018.
(89) Zhao, Y.; Truhlar, D. G. A new local density functional for main-group thermochemistry, transition metal bonding, thermochemical kinetics, and noncovalent interactions. *J. Chem. Phys.* **2006**, *125*, 194101.
(90) Brown, C. J.; Sadanaga, R. The crystal structure of benzil. *Acta Crystallogr.* **1965**, *18*, 158−164.
(91) Odou, G.; More, M.; Warin, V. Etude Cristallographique de la Transition de Phase du Benzil. *Acta Crystallogr.* **1978**, *34*, 459−462.
(92) Gabe, E. J.; Page, Y. L.; Lee, F. L.; Barclay, L. R. C. The structure of 2,2',4,4',6,6'-hexa-tert-butylbenzil. *Acta Crystallogr.* **1981**, *B37*, 197−200.
(93) More, M.; Odou, G.; Lefebvre, J. Structure Determination of Benzil in its Two Phases. *Acta Crystallogr.* **1987**, *43*, 398−405.
(94) Charpe, V. P.; Sagadevan, A.; Hwang, K. C. Visible light-induced aerobic oxidation of diarylalkynes to α-diketones catalyzed by copper-superoxo at room temperature. *Green Chem.* **2020**, *22*, 4426−4432.
(95) Kanagathara, N.; Senthilkumar, K.; Sabari, V.; Ragavendran, V.; Elangovan, S. Structural and Vibrational Investigation of Benzil-(1,2-Diphenylethane-1,2-Dione): Experimental and Theoretical Studies. *J. Chem.* **2022**, *2022*, 5968496.
(96) Bhukta, S.; Chatterjee, R.; Dandela, R. Metal-free, 2-MeTHF mediated C(sp)−H functionalization of alkynes with anilines to access diaryl 1,2-diketones bearing lower E-factors. *Green Chem.* **2023**, *25*, 3034−3039.
(97) Guner, V.; Kabak, M.; Elerman, Y. Structure and conformation of 2,3,4-triphenyl-1-oxa-4-azabutadiene. *J. Mol. Struct.* **2000**, *526*, 151−157.
(98) Fukuyo, M.; Hirotsu, K.; Higuchi, T. The structure of aniline at 252 K. *Acta Crystallogr.* **1982**, *38*, 640−643.
(99) Lewis, G. N. The Atom and The Molecule. *J. Am. Chem. Soc.* **1916**, *38* (4), 762−785.
(100) Weinhold, F.; Landis, C. *Valency and Bonding, a Natural Bond Orbital Donor-Acceptor Perspective*; Cambridge University Press: Cambridge, UK, 2005.
(101) Altun, A.; Neese, F.; Bistoni, G. Effect of Electron Correlation on Intermolecular Interactions: A Pair Natural Orbitals Coupled Cluster Based Local Energy Decomposition Study. *J. Chem. Theory Comput.* **2019**, *15* (1), 215−228.
(102) Parker, T. M.; Burns, L. A.; Parrish, R. M.; Ryno, A. G.; Sherrill, C. D. Levels of symmetry adapted perturbation theory (SAPT). I. Efficiency and performance for interaction energies. *J. Chem. Phys.* **2014**, *140* (9), 094106.
(103) Bader, R. F. W.; Nguyen-Dang, T. T.; Tal, Y. A topological theory of molecular structure. *Rep. Prog. Phys.* **1981**, *44*, 893−948.
(104) Bader, R. F. W. Comment on the Comparative Use of the Electron Density and Its Laplacian. *Chem.—Eur. J.* **2006**, *12*, 7769−7772.
(105) Popelier, P. L. A. On the full topology of the Laplacian of the electron density. *Coord. Chem. Rev.* **2000**, *197*, 169−189.
(106) Bone, R. G. A.; Bader, R. F. W. Identifying and analyzing intermolecular bonding interactions in van der Waals molecules. *J. Phys. Chem.* **1996**, *100*, 10892−10911.
(107) Espinosa, E.; Alkorta, I.; Elguero, J.; Molins, E. From weak to strong interactions: A comprehensive analysis of the topological and energetic properties of the electron density distribution involving X−H···F−Y systems. *J. Chem. Phys.* **2002**, *117*, 5529−5542.
(108) Sen, S.; Sinha, A.; Banerjee, S.; Debnath, S.; Ghosh, A.; Chakraborty, J.; Gangopadhyay, J. Noncovalent and Covalent O-H...O Interactions in PPh_3O Cocrystals: A Correlation Study Involving QTAIM, SAPT, NBO, and IBSI Methods. *ACS Omega* **2024**, *9*, 22476−22487.
(109) Sinha, A.; Sen, S.; Ghosh, A.; Mukherjee, S.; Banerjee, S.; Gangopadhyay, J. Delving into the ambiguity in lattice site assignment of aquo-H atom in the orthorhombic PPh_3O.hemihydrate: A comparative account of three PPh_3O. hemihydrate polymorphs. *Results Chem.* **2024**, *10*, 101710.
(110) Lefebvre, C.; Khartabil, H.; Boisson, J.-C.; Contreras-García, J.; Piquemal, J.-P.; Hénon, E. The Independent Gradient Model: A New Approach for Probing Strong and Weak Interactions in Molecules from Wave Function Calculations. *ChemPhyschem* **2018**, *19*, 724−735.

https://doi.org/10.1021/acsomega.4c07702
ACS Omega 2024, 9, 45518−45536